

Time-resolved imaging of model astrophysical jets

THEODOROS SMPONIAS¹

¹Ioannina, Greece.

Abstract. An approximate, time-delayed imaging algorithm is implemented, within existing line-of-sight code. The resulting program acts on hydrocode output data, producing synthetic images, depicting what a model relativistic astrophysical jet looks like to a stationary observer. The software has the potential to study a variety of dynamical astrophysical phenomena, in collaboration with other imaging and simulation tools. A number of tests are performed, in order to confirm the validity of code results, and also to present the features of the software. The above demonstrate the potential of the computer program to help interpret astrophysical jet observations.

Keywords. ISM: jets and outflows, stars: winds-outflows, stars: flare, radiation mechanisms: general, methods: numerical.

Math. classification. 85-08.

1. Introduction

Imaging a relativistically-moving macroscopical object, opens a window to a rather unexpected and even strange world of peculiarities. The basic mandates of Special Relativity, regarding length contraction and time dilation, constitute a mere beginning in the quest for comprehension of the actual appearance of a fast-moving object ([14, 19, 21, 28, 33]). Looking at the fast object travelling in front of the eye, or the telescope, an observer shall *see* the object view affected by a number of relativistic distortions ([2, 30, 31]).

In order to simulate the observation of a relativistic astrophysical jet (for example [16]), a model needs to include a stationary observer, and a fast-moving gaseous mass, the latter comprising both the jet, and some of its surrounding matter, being dragged and pushed along with it. The transformation of electromagnetic emissions from the jet's own frame of reference ('fast moving frame') to the Earth frame ('stationary frame') requires performing the Lorentz/Poincaré transform ([1, 7, 30, 32]). Applying the aforementioned transform for imaging purposes, aims to reconstruct what the observer will actually see, as opposed to what is measured. Relevant to this point, [9] argues about the important difference between vision and measurement in Special Relativity, presenting the aforementioned difference in a geometrical manner.

Radiation emitted from a jet is therefore subject to relativistic effects ([7, 20]), including time dilation, relativistic aberration and frequency shift, leading collectively to what is known as Doppler boosting or relativistic beaming ([8, 30, 32]). Aberration causes the fast-moving object to actually appear *rotated* to a stationary observer ([3, 19, 28, 30]), a phenomenon sometimes called the Terrell-Penrose rotation.

[5, 6] provide an early computerized attempt to reconstruct a relativistic image, through the eyes of an observer crossing a scene at high velocity. [12] demonstrates the importance of the relativistic transform of brightness and color. When imaging a jet, these correspond to Doppler boosting and frequency shift, respectively. [12] discusses an object that moves at uniform speed across the field of view, but is visually large enough for the angle between velocity and line of sight to vary along the object. Applying the Lorentz transform changes brightness and color in a separate manner, for each point of the observed object. [30] improves on such calculations, providing various methods for relativistic visualization, in both Special and General relativistic frameworks.

[18] calculate the visual appearance of wireframe relativistic objects, by mathematically inverting the course of light from an image point to the emission event. They provide expressions that directly describe how a series of objects would look like, when moving at high speed, in front of a stationary observer. The efficiency of their method is then compared to the increased detail of a related ray-tracing project ([17]). [8] image scenes with a fast observer traveling through their artificial environment. They also relate their simulations to actual imaging experiments, using the femto-photography technique ([29]). Furthermore, they introduce a number of additional details into their models, such as camera distortions from traveling at very high speed. [22] present an important framework, where the subject of relativistic imaging is explored in a scientifically correct but also accessible manner.

Even though ray-tracing methods provide excellent quality of relativistic images, they still lack in efficiency, when compared to other methods, such as polygon rendering ([31]). In the current paper, a hybrid relativistic imaging method is presented, whereby time-resolved hydrocode data are being crossed by lines of sight (LOS), parallel to each other. Most relativistic effects are directly incorporated, the rest being represented approximately. Some accuracy is thus traded for increased efficiency, allowing for near-real time relativistic imaging of evolving model jets, with modest computing resources.

In the remaining of this paper, the methodology used in the imaging process, in order to draw the synthetic image, is presented first (Section 2). We then proceed to briefly describe the new code itself, called RLOS (Relativistic Line Of Sight) (Section 3). The code tests are then provided, where the imaging process is executed repeatedly, with different settings, based on just a few underlying hydrocode runs. Through artificially altering certain parameters in post-processing, the imaging code behaviour under different circumstances is explored and results are discussed (Section 4). Finally, in Section 5 useful conclusions are drawn from the current work and possible future applications for the imaging code are proposed.

2. Implementation

2.1. 3-dimensional imaging

Previous, non-relativistic imaging code, (employed by [11,25,26]) works as follows: For each pixel of the "imaging" side of the 3D computational domain (Figure 1), a line of sight (LOS) is drawn, beginning from that pixel, through the imaged volume. Along the LOS, the equation of radiative transfer is solved at each cell, using localized emission and absorption coefficients. Depending on the situation modelled, the emission coefficient may be either calculated directly, or outsourced to another program.

Lines of sight are drawn starting from a pixel of the yz-side or xz-side (either way called the imaging side) of the domain, tracing their way (Figures 1 and 2) along the given direction, until they reach a length of $\sqrt{(x_{max}^2 + y_{max}^2 + z_{max}^2)}$, where $x_{max}, y_{max}, z_{max}$ are the dimensions, in cells, of the computational domain. In practice, on reaching the end of the domain, either 'top' or 'side', they stop calculating, therefore some LOS's end up shorter than the maximum length.

The above process is then repeated within a 2D loop, running over the imaging plane, each LOS corresponding to a single pixel of the final synthetic image. Along a LOS, no sideways scattering is considered. It is in the above manner that the synthetic image is created. The latter image is therefore drawn on the plane of origin of the LOS's, constituting a parallel displacement of itself from the plane of the observing eye, LOS's being parallel to each other.

The 3D setup of RLOS remains very similar to that of its ancestor classical imaging code. Consequently, Figures 1 and 2 depict the 3D geometrical arrangement, common for both classical and relativistic LOS code.

The geometric description of a model astrophysical system may be inserted into RLOS directly, for example forming a 'conical' jet setup ([4]), which is already implemented in an inactive part of the

TIME-RESOLVED JET IMAGING

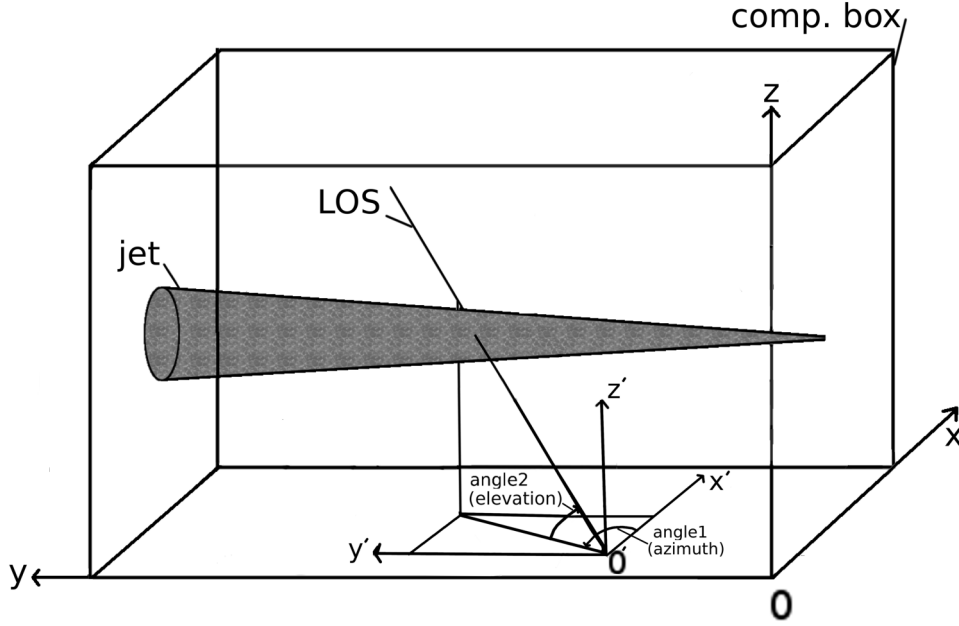


FIGURE 1. A schematic view of the 3D spatial geometric arrangement of line-of-sight imaging code, specifically applied to a model astrophysical jet. The imaging side of the computational box here is the yz plane, located on the side of the box apparently closer to the reader. Lying on the aforementioned yz plane, O' is the point of origin of a random LOS, with its own dashed coordinate system $x'y'z'$. The imaging plane may also lie on the xz side of the computational box. The final image is formed on the eye or detector of a fiducial observer, situated at the end of the LOS, through parallel transport.

program. Alternatively, data output from a hydrocode may be employed, which is actually the case in the current paper, using data from PLUTO ([15]).

2.2. Time-resolved imaging

2.2.1. Accessing the 4-dimensional data

The finite nature of the speed of light affects the appearance of a fast-moving object in a crucial manner. Consequently, drawing a relativistic image of an astrophysical system, necessitates the availability of information regarding not only its spatial characteristics (such as xyz data), but also about its temporal evolution as well. In practice, when executing the PLUTO hydrocode, before running RLOS, we should carefully pre-select the temporal density of hydrocode snapshots, to be saved to disk at regular intervals. The smaller those intervals, the better the temporal resolution of hydrocode data. A series of snapshots shall then be loaded to RAM memory by RLOS, which therefore requires a multiple quantity of RAM, in order to run properly, than either the corresponding PLUTO run, or the classical LOS code. The denser (in time) the data saves loaded into RAM, the higher the amount of RAM needed by RLOS, for a given hydrocode simulation.

An alternative approach considered was to access the different temporal slices directly from disk (using an SSD drive), resulting in using approximately only as much RAM as non-relativistic imaging code. Nevertheless, this line of thought was abandoned, due to the added complexity and relative lack of performance. The current implementation simply loads data from many time instants to RAM and

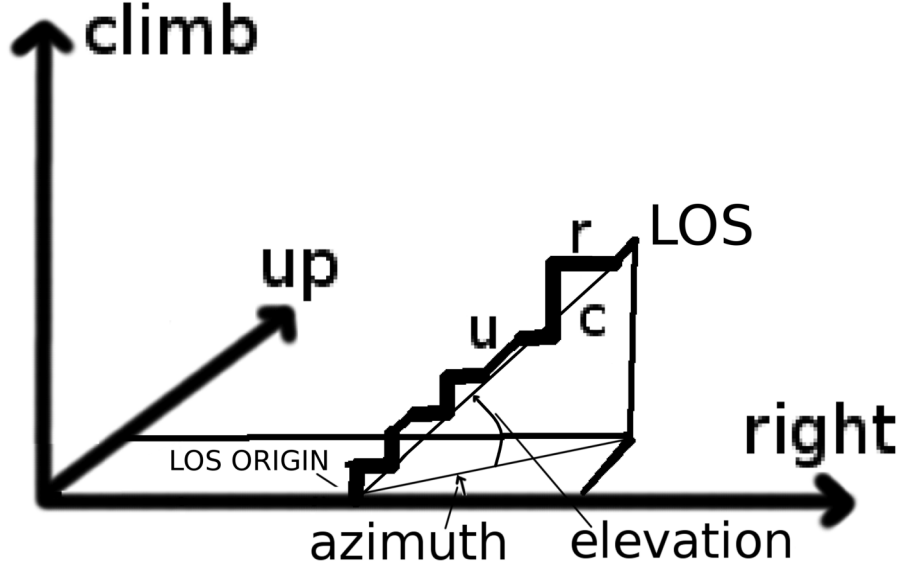


FIGURE 2. A schematic of the spatial propagation of the line of sight (LOS) through the 3-dimensional cartesian computational grid. In the discrete grid, according to the design of the algorithm, there are 3 available directions to be taken at each step along the LOS: *right*, *up* and *climb*. These correspond to x, y and z, respectively. During propagation, the LOS 'tries' to follow its given direction, as defined by the two angles of azimuth and elevation. More specifically, every two steps a decision is first made on azimuth, either right or up. Then, for elevation, it is either climb, or another azimuth decision. In the Figure, along the LOS, horizontal steps point to the 'right' direction. Diagonal steps represent 'up' steps, while vertical steps constitute 'climb' steps.

then works with them. Time is generally counted in simulation time units, since these are read by PLUTO's attached pload routine, which loads PLUTO data into RLOS.

The total data time span available to a LOS, $\Delta t_{LOS(total)} = t_{(last-shot)} - t_{(first-shot)}$ ¹, is consequently measured in simulation time units. $\Delta t_{LOS(total)}$ should be preset to be larger than the light crossing time of the model system, at the selected LOS angle settings. The wider the total time span of hydrocode snapshots loaded into RAM (as measured in simulation time units, *not* merely in number of snapshots), the surer we are that the code will not run out of time instants to access when calculating along a LOS. The total time span available to the LOS can be smaller for a LOS perpendicular to the jet axis, and should be larger for a LOS traversing the jet nearly parallel to its axis.

Documenting the model jet evolution generally requires hydrocode data saves to be rather dense in time. A finer temporal resolution of the data is therefore important, especially for fast-changing flows. On the other hand, a lower temporal resolution will probably suffice for a steadier, slower-paced flow. The total number of snapshots used are therefore a tradeoff parameter to be adjusted carefully, in order to preserve precious RAM memory, thus allowing for higher *spatial* resolutions to be achieved, for a given RAM quantity available on a computer.

2.2.2. Traversing the 4D spatio-temporal arrays

Introduction. As mentioned above, in order to execute the code, a series of PLUTO data snapshots are loaded to RAM memory from beforehand, populating the elements of 4-dimensional (4D) arrays,

¹Not to be confused with the interval Δt_{shot} between *successive* snapshots

TIME-RESOLVED JET IMAGING

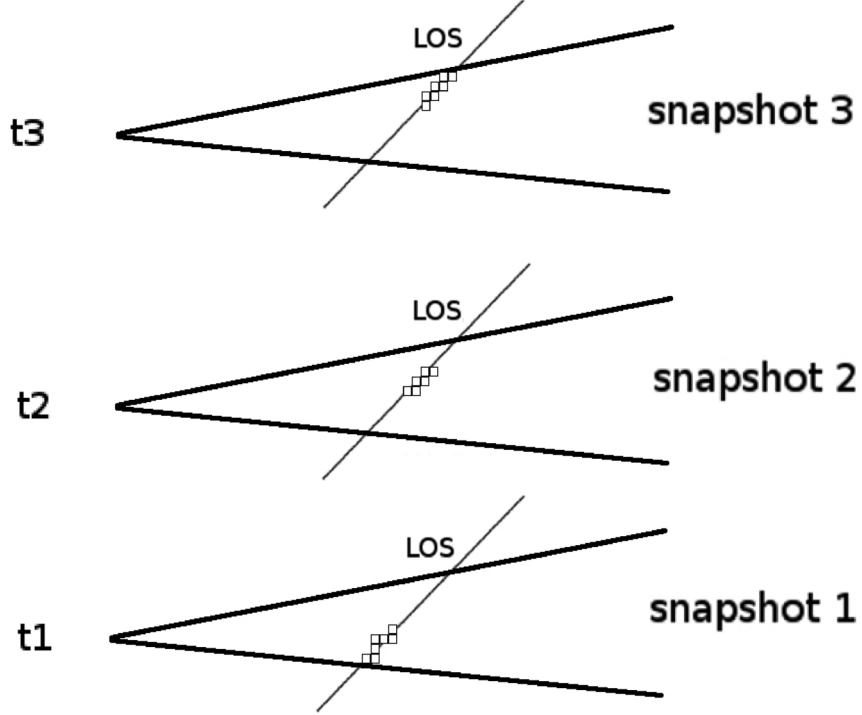


FIGURE 3. At regular intervals, we jump to a new temporal 3D slice of a 4D spacetime array, obtaining a discrete approximation of the time continuum, in the form of the PLUTO hydrocode snapshots.

called spacetime arrays. From a *temporal* point of view, the RLOS code shall then begin its run from the PLUTO simulation time corresponding to the first of the aforementioned PLUTO snapshots, called *shotmin*, where $\text{shotmin} \geq 1$. From a *spatial* point of view, the origin of the RLOS run is located at the first point of the imaging plane, which is a specific side of the 3D computational box (Figure 1). As the calculation advances, in 3D space, along the LOS being drawn (Figure 2), the algorithm keeps checking whether to jump to a new *temporal* slice, while staying 'on target' in 3D space (Figure 3). Consequently, the ray-tracing algorithm advances in time, through the data (Figure 4), by sequentially accessing successive instants from within the 4D spatiotemporal data arrays.

Time-resolved imaging calculations. For every LOS, we have a point of origin (POO), located on the "imaging side" of the 3D computational grid (Figure 1). That point, addressed in the code as $(nx10, ny10, nz10)$ and here as O' , is the beginning of the LOS's axes x' , y' , z' , parallel to x , y , z respectively. In direct analogy to classical LOS code (Section 2.1), there is a 2D loop, running over the imaging side of the computational box, where the LOS' POO successively locates itself at each point of that box side.

Within each step of the aforementioned 2D loop, as we progress along a LOS, a record is kept of where we are, in 3D space. This record comprises the LOS's own integer coordinates, rc , uc , and cc , measured from its POO. The above symbols stand for right-current, up-current and climb-current, representing the current LOS advance in the x' , y' and z' axes, respectively (Figures 1 and 2). Thus, the current ray position in the grid is $(nx10+rc, ny10+uc, nz10+cc)$.

A timer variable, *curtime* (standing for current LOS time), is introduced for each LOS, facilitating the recording of the duration of insofar ray travel along the LOS. The aforementioned timer is preset

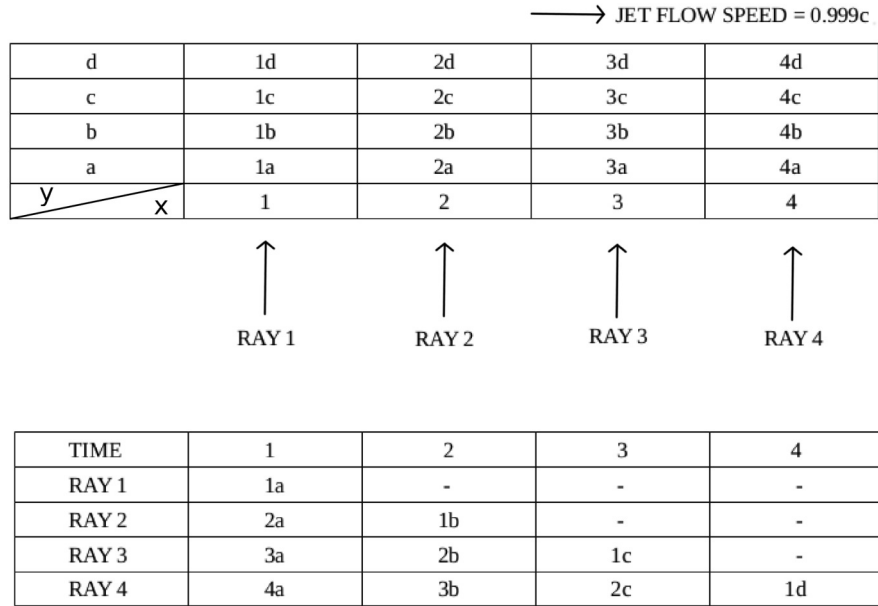


FIGURE 4. Simultaneous advance, in both space (2D) and time, of a few lines of sight. Top half depicts the spatial situation at $t=1$. Sixteen jet matter portions currently occupy this mini 4 by 4 grid. Each piece of matter is named after its position at $t=1$ and retains that name as it moves along. The bottom half shows how the situation evolves as time marches on, with light rays meeting different jet segments that cross their path. A dash means a light ray meeting jet matter other than the above, or nothing at all.

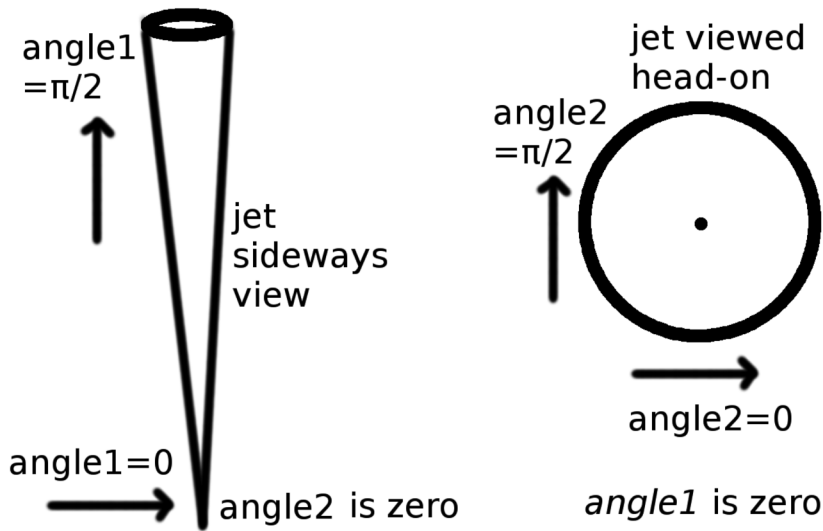


FIGURE 5. The geometric arrangement with regard to the viewing angles in the model, for the special cases of $\text{angle2} = 0$ (left) and $\text{angle1} = 0$ (right). For each sub-case, the arrow shows the direction of the LOS, which is different than the reader's direction of view.

TIME-RESOLVED JET IMAGING

at the beginning of each LOS, to the hydrocode time of the first data snapshot, from the pre-set series of snapshots already loaded to RAM.

We then proceed to calculate the current length of the LOS, through the following formula:

$$l_{los(current)} = [(dlr * (nx1current - nx10))^2 + (dlu * (ny1current - ny10))^2 + (dlc * (nz1current - nz10))^2]^{1/2} \quad (2.1)$$

$$+ (dlc * (nz1current - nz10))^2]^{1/2} \quad (2.2)$$

where the LOS length is measured in cell length units and

$$nx1current = nx10 + rc \quad (2.3)$$

$$ny1current = ny10 + uc \quad (2.4)$$

$$nz1current = nz10 + cc \quad (2.5)$$

dlc, dlu, dlr are the *normalized* hydrocode cartesian cell lengths along the x, y and z directions, respectively. Their values are usually unity, or close to unity, as set in the hydrocode by the user, and have to be the same all over the grid, meaning only homogeneous grids are currently supported. Furthermore, if the hydrocode grid is read, by pload, at a reduced resolution, then RLOS cell sizes are automatically adjusted accordingly.

We can finally write

$$l_{los(current)} = [((dlr * rc)^2) + ((dlu * uc)^2) + ((dlc * cc)^2)]^{1/2}$$

From a temporal point of view, the first of the snapshots loaded to RAM initially becomes the current snapshot, i.e. its temporal slice of the 4D data arrays is now being accessed by RLOS.

We then proceed to calculate curtime, the current time of the light ray along the LOS, to be used in order to determine the suitable temporal slice of the 4D arrays

$$curtime = l_{los(current)} / c_{light} + t_{0(LOS)} \quad (2.6)$$

where $t_{0(LOS)}$ is when the LOS begins to be drawn, from its point of origin. In practice, this is the timestamp of the first loaded snapshot. The parameter c_{light} is the speed of light, expressed in cells per simulation second.

When the current LOS time exceeds the next snapshot's timetag, then the algorithm switches to drawing the LOS through the 3D volume of the next available snapshot (next temporal slice of the 4D data arrays) (Figure 3).

We keep moving along the same LOS in 3-D space, but we have just shifted to a new instant in the time records of the hydrocode. Consequently, we are now traversing the next temporal slice of the 4-D spatio-temporal data arrays.

The above temporal shift is repeated as many times as required by the relevant criterion along the LOS, until the spatial end of the LOS is reached. The closer to each other, in time, the stored successive hydrocode snapshots are, the more accurate the time-delayed imaging approximation becomes, subject to existing hardware constraints of available RAM.

2.2.3. Aiming the line of sight

The direction of a LOS in 3D space is defined by the two angles of azimuth (angle 1) and elevation (angle 2) (Figure 1). The plane of angle 1 is the x'y' plane, parallel to the xy one. Angle 2 is perpendicular to angle 1. For a jet moving parallel to the y axis, the angle between the local jet matter

velocity \vec{u} , and the LOS, called $losu$, is often (mainly when u is parallel to the jet axis) small, when angle 1 approaches 90 degrees, and vice versa (left half of Figure 5). As is well known ([7]), it is the angle $losu$ that matters in the relativistic emission calculations.

Short of jet precession occurring, the plane of angle 2 (elevation) is largely perpendicular to the jet when angle 1 is zero, while it is roughly parallel to the jet when angle 1 is 90 degrees. Usually, the jet bears an approximate cylindrical symmetry, meaning that for a small angle 1, by varying angle 2, we mainly rotate the view around the jet axis, producing similar intensities throughout the way, viewing the jet as if from along a ring around the jet axis (right half of Figure 5). In summary, for a roughly cylindrical hydrojet moving along the y axis, the smaller angle 1 is, the less difference varying angle 2 makes.

On the other hand, for angle 1 nearing $\pi/2$, varying angle 2 rotates the view approximately within the yz plane that is roughly parallel to the jet. Consequently, the larger angle 1 is, the stronger the effect, on the synthetic image, from changing angle 2.

2.3. Relativistic Effects

The main effects of the Lorentz/Poincaré transform on the emission from a relativistic object ([30]), specifically applied to an astrophysical jet, are relativistic aberration, time dilation and frequency shift ([1, 7, 13, 27]).

2.3.1. Lorentz factor

The Lorentz factor for a hydrocode cell is ([7])

$$\Gamma_{Lorentz} = \frac{1}{\sqrt{1 - v_{total}^2}} \quad (2.7)$$

where, in our case

$$u_{total} = \sqrt{u_x^2 + u_y^2 + u_z^2} \quad (2.8)$$

is the local velocity and all speeds are in units of the speed of light, with a maximum value of 1.

2.3.2. Doppler factor calculation

In the effect of Doppler boosting (DB), radiation is either boosted or de-boosted, depending on the angle $losu$, formed in 3D space, between the direction of the LOS and the local velocity vector, \vec{u} . The closer we are to observing the jet head-on (average $losu$ getting smaller), the stronger the boosting becomes. In addition, the higher the jet speed, the narrower and the stronger the boost cone around the jet head direction. On the other hand, outside the boost cone, *de*-boosting occurs, that is to say the higher the velocity is, the weaker the signal becomes. Within RLOS, Doppler boosting is obtained from the expression ([7]):

$$D_{factor} = \frac{\sqrt{1 - u^2}}{(1 - u * \cos(losu))} \quad (2.9)$$

The cosine of the angle $losu$ is calculated, in the following manner:

Let us define ($L\vec{O}S$), a fiducial unitary vector, pointing along the preset direction of the LOS's. Furthermore, let ($lx1, lx2, lx3$) be its components, while (u_x, u_y, u_z) are the velocity components along the corresponding axes.

TIME-RESOLVED JET IMAGING

For the local jet matter velocity we therefore have

$$\vec{u} = (u_x, u_y, u_z) \quad (2.10)$$

and as we know (equation 2.8)

$$u = \sqrt{u_x^2 + u_y^2 + u_z^2} < 1 \quad (2.11)$$

and

$$L\vec{O}S = (lx1, lx2, lx3) \quad (2.12)$$

where

$$(LOS) = \sqrt{lx1^2 + lx2^2 + lx3^2} = 1. \quad (2.13)$$

In the following, ϕ_1 and ϕ_2 represent angle 1 and angle 2, respectively.

$$lx1 = \cos(\phi_1)\cos(\phi_2) \quad (2.14)$$

$$lx2 = \sin(\phi_1)\cos(\phi_2) \quad (2.15)$$

$$lx3 = \sin(\phi_2), \quad (2.16)$$

where both angles are known, and are fixed for parallel lines of sight. We now have

$$L\vec{O}S * \vec{u} = (LOS) * u * \cos(\widehat{L\vec{O}S, \vec{u}}). \quad (2.17)$$

Alternatively,

$$L\vec{O}S * \vec{u} = lx1 * u_x + lx2 * u_y + lx3 * u_z \quad (2.18)$$

Therefore, from equations 2.17 and 2.18, we have

$$\cos(\widehat{L\vec{O}S, \vec{u}}) = \frac{lx1 * u_x + lx2 * u_y + lx3 * u_z}{(LOS) * u} \quad (2.19)$$

Consequently, from equations 2.11, 2.13 and 2.19 we obtain

$$\cos(\widehat{L\vec{O}S, \vec{u}}) = \frac{lx1 * u_x + lx2 * u_y + lx3 * u_z}{\sqrt{(u_x^2 + u_y^2 + u_z^2)}} \quad (2.20)$$

Where lx1, lx2 and lx3 are known from equations 2.14, 2.15 and 2.16. In practice, a miniscule number is added to the denominator of Eqn. 2.20, in order to avoid possible division by zero, if $u=0$. This does not affect the result considerably, while making the code more stable to run.

The above calculation allows the assignment of a Doppler boosting factor, through equations 2.9, 2.11 and 2.20, to each discrete emission event along a line of sight, depending on the angle between the local velocity in the cell and the LOS, and on the value of the local velocity itself.

2.3.3. Doppler boosting

The combined imaging effect can be expressed in total as ([1, 7])

$$S_{obs} = S_{jet}^{3+\alpha} \quad (2.21)$$

where α is the spectral index for the jet spectrum. The exponent, $(3+\alpha)$, in the above can be broken down into different contributions from separate effects. 2 units come from the aberration of light, 1 unit from the relativistic dilation of time and the α comes from the effect of frequency shift. The above are briefly analyzed in what follows. For a continuous optically thin jet we may lose a D factor from the above ([1], see also below this Section).

Frequency shift. Radiation emitted at a given frequency, from a fast-moving jet fluid portion is taken to be Doppler shifted in frequency

$$f_{obs} = f_{calc}D \quad (2.22)$$

where f_{obs} is the observed frequency and f_{calc} is the frequency used in the emission calculations, which are done in the jet frame of reference ([7]). Regarding intensity, we employ an implied power-law spectrum falling off with frequency, of the form

$$S_f \simeq S_f^{-\alpha} \quad (2.23)$$

where α is the spectral index, assumed, as an approximation, in this paper to take the value of $\alpha = 2.0$, a value generally referring to the optically thin region of the jet. For $D \geq 1$, emission is calculated at a frequency lower than the observed, resulting to a higher intensity, since the spectrum employed generally falls off with frequency. In the code, this emission effect is included in the Doppler boosting formula.

$$\alpha = -\frac{d \ln S'_f}{d \ln f} \quad (2.24)$$

Consequently,

$$\frac{S_{obs}}{S_{calc}} = D^\alpha \quad (2.25)$$

Furthermore, the code may include in the future an emission model dependent on frequency, where we calculate emissions at f_{calc} and observe that at f_{obs} , without the need to include the D^α factor any more.

At the moment, the frequency shift effect is included only as a quantitative indicator, where intensity is multiplied by the square of the ratio $n_{gen}/n_{obs} = 1/D^2$, partially negating the aforementioned effect of spectrum-related boosting.

Aberration-searchlight effect. Relativistic aberration changes the perceived direction of light, when transforming between the jet frame and the earth frame, 'tilting rays', emanating from the jet, towards its head area. The resulting path of light is nevertheless *measured* to be identical in both frames of reference ([30], section 4.6.1). As an approximation, we opted to forgo this effect geometrically, only employing straight lines of sight. In order to compensate for the above simplification, the two Doppler factors, representing aberration, are employed in the Doppler beaming formula.

Normally, the focusing of the beam forward, for a jet approaching head-on, would occur automatically from the program, no D^2 needed. But in our case, instead of focusing the sidereal rays to the front, while diluting those to the side, we simply multiply the intensity of each emission event, along each ray, by the event's own D^2 . D tends to be smaller to the sides, and larger towards the jet direction. Rays within the boost cone are then reinforced accordingly, while others are weakened. This constitutes an approximation that reduces the complexity of code setup (all rays are parallel) and also its computational load demand. Even though some detail is hitherto missed from the images, as we do not concentrate sidereal LOS rays to the jet head, this approximation allows for more efficient jet imaging.

Time dilation. Time dilation contributes one D factor to the emission result.

2.4. Testing parameters

In this area, we shall present certain parameters that facilitate testing the code.

TIME-RESOLVED JET IMAGING

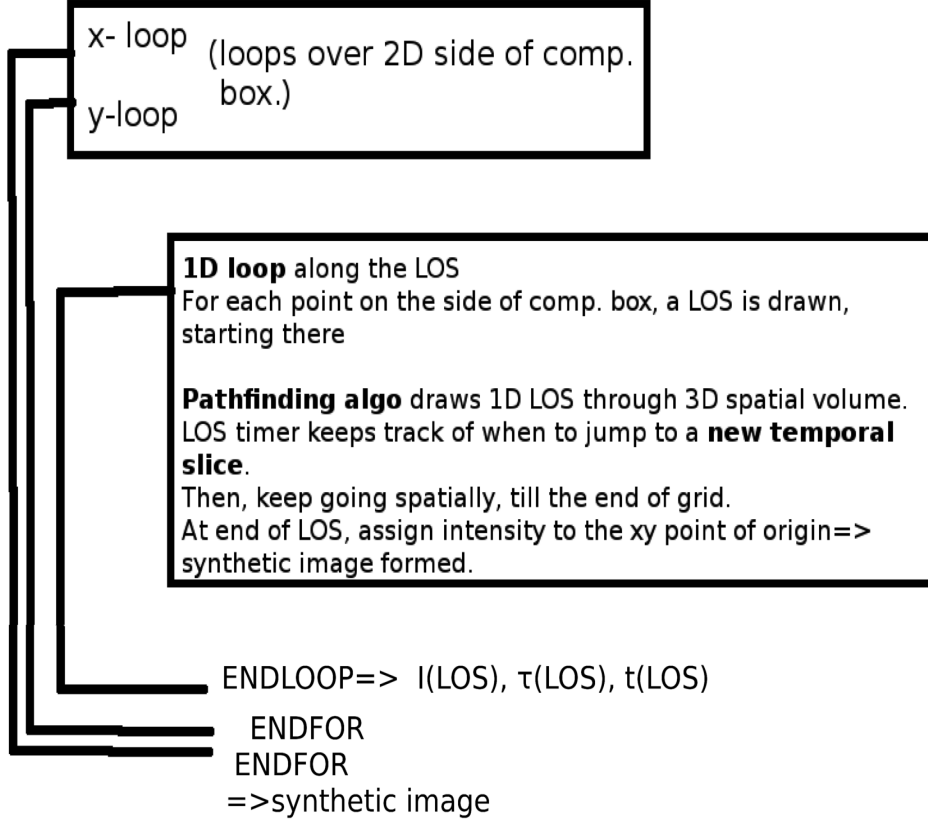


FIGURE 6. A simplified flow diagram depicting the basic logical structure of RLOS imaging code. The synthetic image's xy loops here correspond to either the yz or the xz side plane of the computational box.

2.4.1. The *clight* parameter

A parameter that expresses the speed of light in cells per unit of time, called *clight*, is introduced. Let us consider a 4D array, comprising a succession of hydrocode snapshots. The LOS traversing those data, naturally moves at a speed of *clight* cells per time unit. When we artificially adjust *clight* to a lower value ([10, 22]), then the algorithm jumps to a new snapshot after spatially advancing through fewer cells, than if *clight* was bigger. A slower LOS advances farther in time while crossing a given distance through the jet, allowing for a detailed study of the time-jumping algorithm.

On the other hand, setting *clight* to a very high value (such as $clight = 400$ for the scale used in this paper), leads to a single shot image, as the RLOS code never jumps to a further temporal slice.

For the PLUTO models used in the sample application run of this paper, the natural value of *clight* is

$$clight = 3 \times 10^{10} \times \frac{t_{PLUTO}}{l_{cell}} = \frac{3 \times 10^{10}}{u_{PLUTO}} = 1 \quad (2.26)$$

where t_{PLUTO} is the hydrocode time unit, $u_{PLUTO}=1$ is the speed of light, in units of c and l_{cell} is the cell length. Furthermore, certain units of measurement employed by the hydrocode are

$$L_{PLUTO} = 10^{10} cm \quad (2.27)$$

$$u_{PLUTO} = 3 \times 10^{10} cm/s \quad (2.28)$$

T. SMPONIAS

$$\rho_{PLUTO} = 1.67 \times 10^{-24} g/cm^3 \quad (2.29)$$

$$t_{PLUTO} = \frac{L_{PLUTO}}{u_{PLUTO}} = \frac{1}{3} s \quad (2.30)$$

$$B_{PLUTO} = \sqrt{4\pi\rho_{PLUTO}u_{PLUTO}^2} = \sqrt{4\pi \times 1.67 \times 10^{-24} \times 9 \times 10^{20}} \simeq 0.137G. \quad (2.31)$$

The cell length in the test simulation is conveniently setup to the value of one model length unit, leading to an intrinsic clight value of 1

$$l_{cell} = 1L_{PLUTO}, \quad (2.32)$$

Therefore, clight is the speed of light in cells/s. The time span, in simulation seconds, between data snapshots, should optimally be set, when preparing the hydrocode run, at $l_{LOS}/(n * clight)$. l is the grid length, in *cells*, along the LOS direction, clight is light speed in cells/(simulation s), and n is the desired number of snapshots to cover the whole imaged timespan. In general, the model is sized to fit a typical microquasar jet system.

If we employ the parameter sfactor, pload's shrink factor, imaging voxels are enlarged and the calculated value of clight shrinks accordingly. The overall accuracy then suffers somewhat, and shrinking the grid should be used only as a preview. Setting sfactor to a value of 2, or more, should therefore provide for a quick preview of the result, while sfactor=1 is the correct option for production runs. The value of clight may be manually overridden by overwriting it through an assignment hardwired into the code.

It must be noted that altering clight only affects the light ray speed, and not the speed of matter. Consequently, meddling with clight does not affect the relativistic emission calculations (like tweak-speed does, Section 2.4.2). An altered clight is merely an artifice, introduced in post processing, in order to explore the effect of using more, or less, temporal slices in the final image.

2.4.2. The speed tweak parameter

For the purpose of examining how altering matter velocity affects the final image, without actually re-running the simulation, a test is introduced, where the above velocity is multiplied, on a global scale (all over the grid), by a 'speed tweak' factor. This offers a quick way to observe the impact of altering the hydrodynamic speed in post-processing, on the synthetic image, for the exact same underlying spatial and temporal matter distribution. The dynamic evolution of the jet is not affected by tweak-speed, the latter only acting in post-processing form on the simulation data.

In contrast, running a different simulation every time, with a different initial jet speed, would have had changed many things, including jet matter distribution, thus obstructing easy and direct comparison between similar simulations at different speeds.

The natural value of tweak-speed is 1. At low tweak speed factors (less than 1) the effects of either DB or FS are reduced, leading to less influence from them on the final image. On the other hand, when tweak-speed is increased, then FS and DB may have an important effect on the synthetic image, depending on the viewing angles and on location. It is important to take care not to raise tweak-speed above the value of $c/u_{(max)}$, or else we obtain errors, since velocities higher than c are then artificially created in the computational grid.

2.4.3. The FS switch

In the code, after the hydrodata are loaded, a global operation calculates, for each cell, a different jet frame frequency, from the common observing one

TIME-RESOLVED JET IMAGING

$$f_{calc} = \frac{f_{obs}}{D_{factor}} \quad (2.33)$$

The frequency shift (FS) switch selects between using the local f_{calc} or the global f_{obs} in the emission calculations. In this paper, a simplified form of D^α was employed, in order to simulate an *implied* dependence on frequency. The purpose of the FS facility is to demonstrate how a more complicated user-defined spectrum may be introduced, such as for synchrotron emission (for e.g. [4]). Thereupon, in the current work the model is more accurate when FS is switched off.

2.4.4. The DB switch

The DB switch offers the option of using the Doppler boosting effect or not. It determines whether one of $D^{3+\alpha}$ or $D^{2+\alpha}$ factors will be employed, or nothing at all.

2.4.5. An example

As an example, we distinguish four different combinations of DB and FS, as used in this paper. Emissivity is measured in arbitrary units, common for all cases.

1. Both DB and FS turned on.

$$emiss_{FD} = \rho D^{3+\alpha} \left(\frac{f_{calc}}{f_{obs}} \right)^2 = \rho D^{1+\alpha} \quad (2.34)$$

2. DB turned on, FS turned off.

$$emiss_D = \rho D^{3+\alpha} \quad (2.35)$$

3. DB turned off, FS turned on.

$$emiss_F = \rho \left(\frac{f_{calc}}{f_{obs}} \right)^2 = \frac{\rho}{D^2}, \quad (2.36)$$

4. DB turned off, FS turned off.

$$emiss_{none} = \rho \quad (2.37)$$

3. Description of RLOS

3.1. Brief code description

RLOS is written for the GDL or the IDL programming languages, and is released under the LGPL licence. It replaces its classical ancestor, as part of a suite of simulation and visualization programs that study astrophysical jets, in a perceived numerical laboratory. The latter combined approach employs a relativistic hydrocode (such as PLUTO), LOS code, the VisIt visualization package, and a number of in-house gamma-ray ([26]) and neutrino emission calculation programs ([23, 24]). The addition of RLOS to the above software suite, aims to reinforce the realism of the imaging part of the calculations. Finally, the modular structure of the program allows the incorporation of more physical effects in the future.

RLOS is organized in two outer spatial loops, running over the imaging plane and an inner 1-dimensional spatial loop, advancing in pairs of steps, one for each angle, running over the length of a LOS. At the innermost lies a *conditional* temporal loop, running over the hydro data time span. The basic structure and flow of the algorithm can be seen in Figure 6. Since much of the required

calculation load is global, it is performed, where feasible, before the loops, in array-oriented operations, in order to improve performance.

3.2. Running the program

In order to run RLOS, the user has 2 different options: either input some of the parameters at runtime, or run using only preset parameters. The latter may be altered by editing the relevant segment near the beginning of the program.

The actual process of running RLOS is performed as follows: First, we change the current directory, within the program, to the hydrodata directory. There, we have already included PLUTO's accompanying IDL routines. What's more, the various remaining paths defined within the code must be set up around the hydrodata directory. Then, we edit the pload routine and add to it two lines, one where we CD to the data directory, and another adding the latter to the path. Then, from within RLOS, we call pload once (e.g. pload,1), ensuring that it positively loads a data snapshot. Then we move to the beginning of the file and compile RLOS, and finally we run it. Initially, there is a selection of manual or hardwired parameter value entry. At stops, we repress run, till we obtain the synthetic image. The user may employ various visualization routines in order to adjust the way results are presented. 2D imaging results may also be output to data files.

3.3. Intended uses

RLOS may be employed in combination with other software, in order to study astrophysical phenomena in a numerical laboratory. The model grid may be imported from a hydrocode, or even setup directly within RLOS, for simpler geometries. Furthermore, the synthetic images may be processed, in order to compare to actual observations. A user may employ the program as is, or expand it in many directions, adapting it to the task at hand.

4. Results

4.1. Model setup

In this Section, RLOS is tested under different circumstances, employing a variety of parameter values, based on just a few different underlying hydrocode runs. This way, the effect of altering each parameter on the final synthetic image is examined. Such post-processing effects, as described in Section 2.4, are applied in order to analyze their impact on the results.

An intermittent model jet, representing a microquasar system, injected at $u_{jet} = 0.26c$, $0.6c$ or $0.8c$ is studied with the RMHD setup of the PLUTO hydrocode, at a uniform grid resolution of $60 \times 100 \times 60$. In all of the model runs the same initial jet density of 10^{10} protons/cm³ is used, 10 times less than the maximum surrounding gas density. Winds comprise an accretion disk wind construct and a stellar wind, which falls off away from the companion star, located off-grid at (400,0,400), while the jet is threaded by a strong confining toroidal magnetic field of $B=400$ simulation units. Blobs are emitted during the first 1.5 out of every 10 time units, for both the $u=0.26c$ and the $u=0.8c$ models, while for the $u=0.6c$ case, the jet is on during the first 5 out of every 50 time units. The simulations were run until at least $t = 750$ simulation time, saving a data snapshot every 15 time units. Taken from the $u=0.6c$ model run, a snapshot of the density is shown in Figure 7, in both 2D and 3D, where we can see the magnetically collimated sequence of plasmoids advancing through surrounding winds.

RLOS was then run, based on the above hydrocode data. In general, a given image is produced having potential access to all available data snapshots after the one set as initial. The imaging process may or may not use all snapshots available to it, depending on the light crossing time of its model segment (potentially adjusted through the clight parameter), and it is not normally forced to stay on

TIME-RESOLVED JET IMAGING

a certain snapshot. The user should avoid trying to load more snapshots than available in the data, or else the hydrocode time array, called T, is not loaded properly, resulting to errors.

The synthetic images are made as *logarithmic* plots of intensity, meaning that even small apparent differences may amount to significant dissimilarity among plots. In general, most intensity comes from the on-axis regions, while less emission originates from lateral areas of the grid.

The value of matter density is mainly employed as an emission coefficient, unless stated otherwise. Furthermore, Doppler boosted intensity in these tests was proportional to D^{3+a} , for an optically thin jet comprising a series of plasmoids ([1]). No self absorption was used, even though the feature is available for future use.

In the current Section, comparisons between different runs of the imaging code are presented, where usually one, and sometimes two, or more, parameters change from run to run. In this manner, the effect of altering a given parameter, on the code output (synthetic image), is isolated and examined. Each run is identified by both its information tag, also present on the corresponding Figure, and by a chessboard-like 2D pair of alpha-numerical coordinates. The latter refer to within the multi-figures (Figures 16, 17, 18, 19, 20, 21, 22), comprising the bulk of RLOS testing results.

We now define the following correspondences:

Process 1 page 1 is shown in Figure 16.

Process 2 page 1 is shown in Figure 17.

Process 2 page 2 is shown in Figure 18.

Process 2 page 3 is shown in Figure 19.

Process 3 page 1 is shown in Figure 20.

Process 3 page 2 is shown in Figure 21.

Process 4 page 1 is shown in Figure 22.

Process 4 page 2 is shown in Figure 23.

Within the above Figures, except the last one, images are labeled using the aforementioned alpha-numerical coordinate system. For the convenience of the reader, the above Figures are also included, magnified, in the Appendix.

The synthetic images are referred to in the following text as follows: (process, or 'batch', number, page number, alphanumeric coordinate, imaging data). For example, (1,1,1A,data) means process 1, page 1, line 1, column A. The 'data' part contains the values of certain imaging parameters, ts standing for tweakspeed, clight for itself, a1 for angle 1, a2 for angle 2, DB for the Doppler boosting switch and FS for the frequency shift switch. smin/max are the first and last among the snapshots employed, respectively. interval is the time span, in hydrocode units, between successive snapshots, B is the value of the injected magnetic field, in MHD hydrocode units, lightjet means the injected jet is lighter than the winds at the jet base, by a given factor, and finally sfactor is the pload shrink factor. The imaging plane is also mentioned (xz or yz), along with the nominal injection speed of the jet matter. All angles are given in radians.

The dynamic range of the intensity plotted was broadly limited, while retaining the same arbitrary units' scale among different test plots. The use of arbitrary units of intensity means *relative* effects of parameter change are sought after in the tests, as opposed to absolute values.

In the Figures of the results, the values of various imaging parameters of interest are annotated. Most of the symbols were explained above, and we note that, in the Figures, phi1 and phi2 are the two angles of azimuth and elevation respectively, The, common for all results, grid size, in cells, is also given in some of the Figures.

Each of the following subsections describes the effects that changing a certain parameter, or even a small group of parameters, has on the synthetic image.

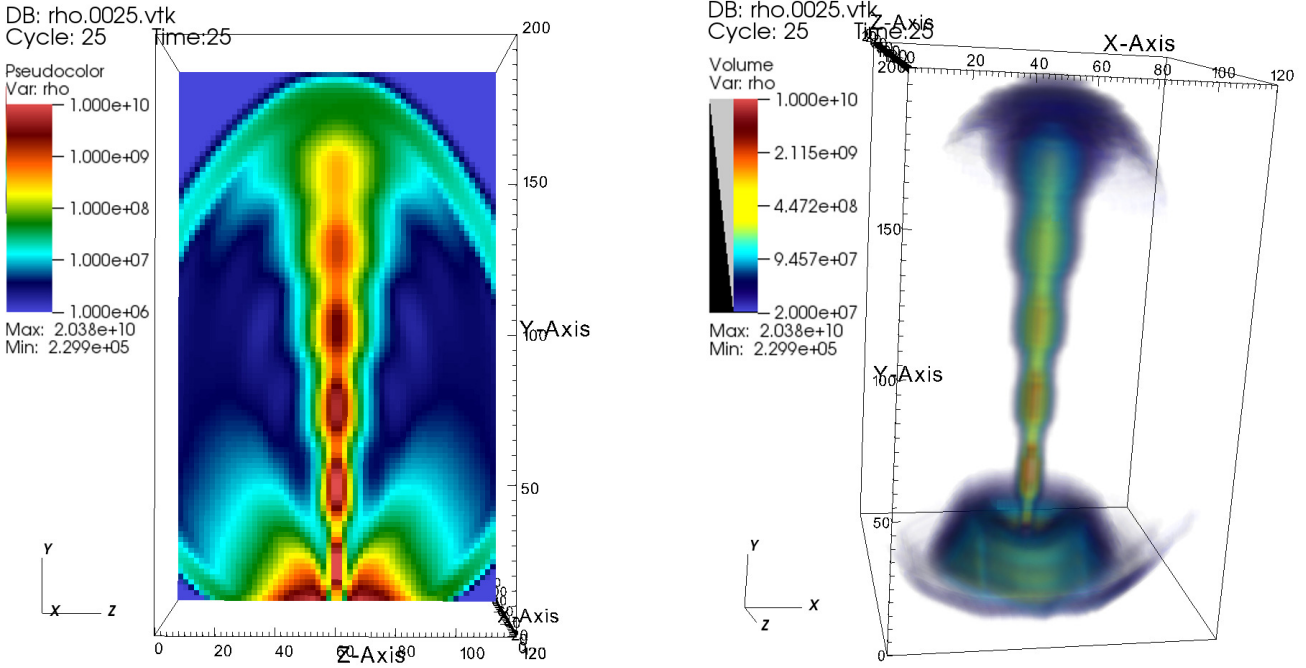


FIGURE 7. Snapshot 25 of the $u=0.6c$ hydrocode run, corresponding to a model time of 375 (25×15), depicting the density. We can see the jet front reaching the end of the grid, having advanced through increasingly lighter surrounding winds, after crossing the simplified accretion disk wind construct. On the left is presented a slice cut through the data and on the right a 3-dimensional density plot. Image produced with VisIt.

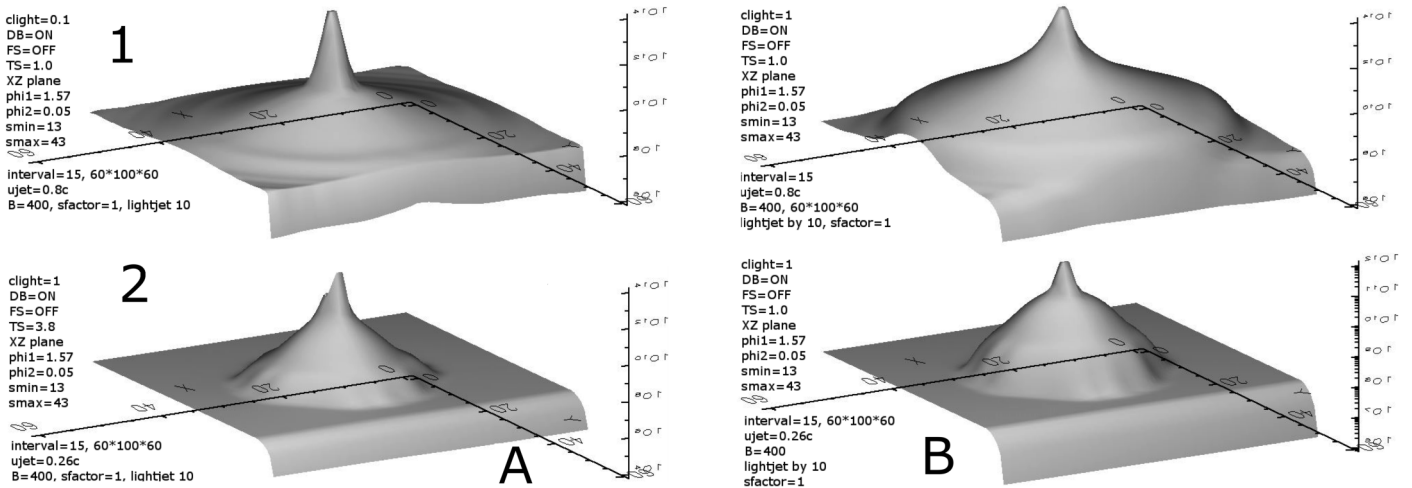


FIGURE 8. First and only part of the first batch of the results.

4.2. Viewing angles

A pair. (process2,page2,1B,ts=1.0,clight=1,a1=0.59,a2=0.005,DB=on,FS=off,smin=37,smax=43,ujet=0.26c,YZ plane,B=400,interval=15,sfactor=1,lightby10) vs

TIME-RESOLVED JET IMAGING

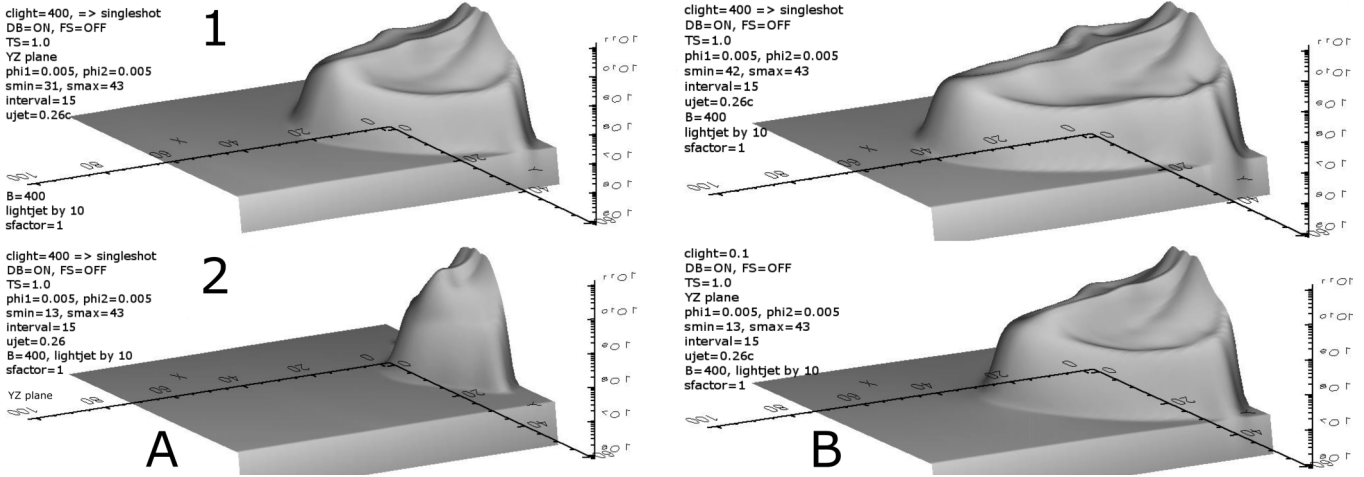


FIGURE 9. First part of the second batch of the results.

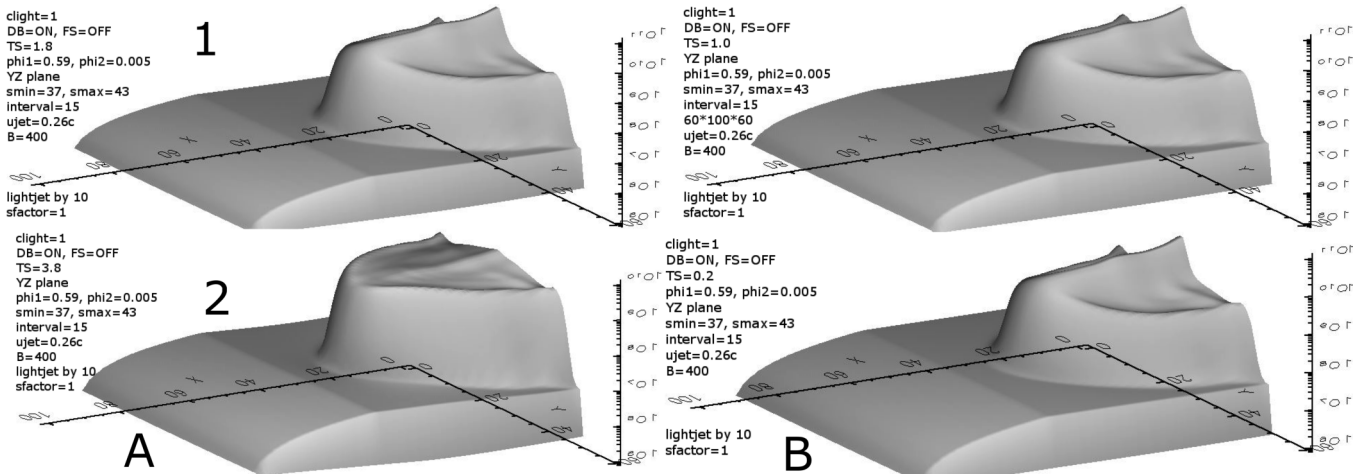


FIGURE 10. Second part of the second batch of the results.

(process2,page3,1A,ts=1.0,clight=1,a1=0.005,a2=0.005,DB=on,FS=off,smin=37,smax=43,ujet=0.26c,YZ plane,B=400,interval=15,sfactor=1,lightby10)

Comment: The effect of varying angle 1 on the synthetic image is apparent here. We can see that when angle 1 is *small*, the LOS is nearly perpendicular to the jet, thus better depicting the object. When angle 1 becomes larger, the image is created somehow off target on the YZ plane, with less image coverage originating from the region of interest. When angle 1 reaches even higher values, approaching $\pi/2$, the jet is observed nearly along its axis. Then, it is time to draw the image on the XZ imaging plane.

A pair. (process4,page1,1A,ts=1.0,clight=1,a1=0.45,a2=0.005,DB=on,FS=off,B=400,smin=18,smax=23,ujet=0.6c,YZ plane,shotmax=4,interval=15,sfactor=1,lightby10) vs

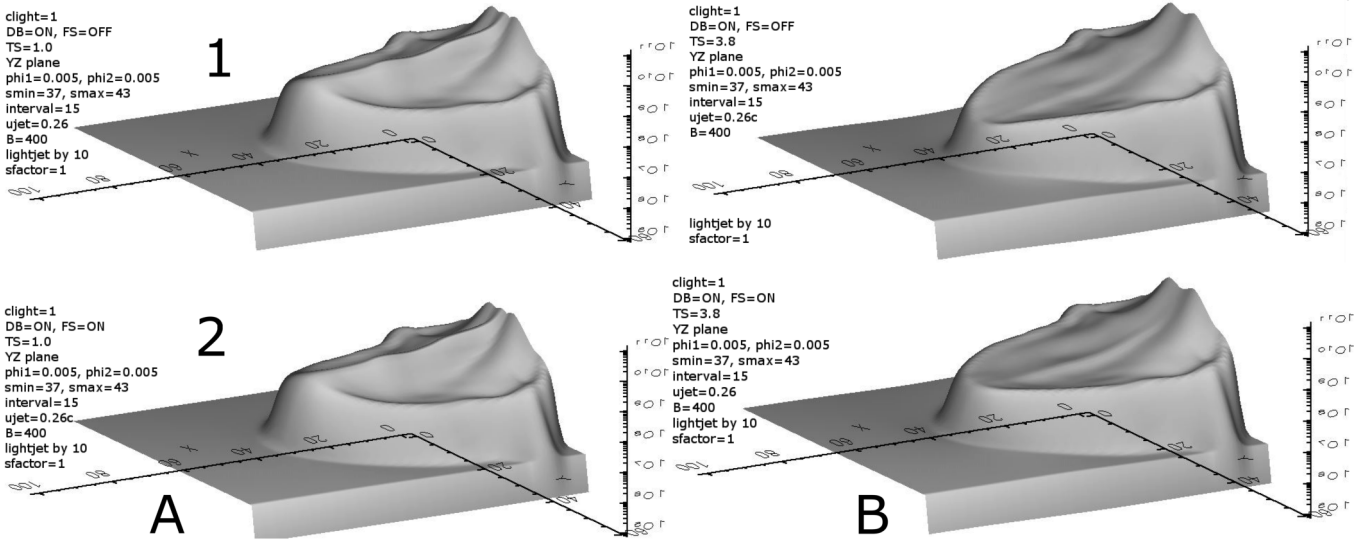


FIGURE 11. Third part of the second batch of the results.

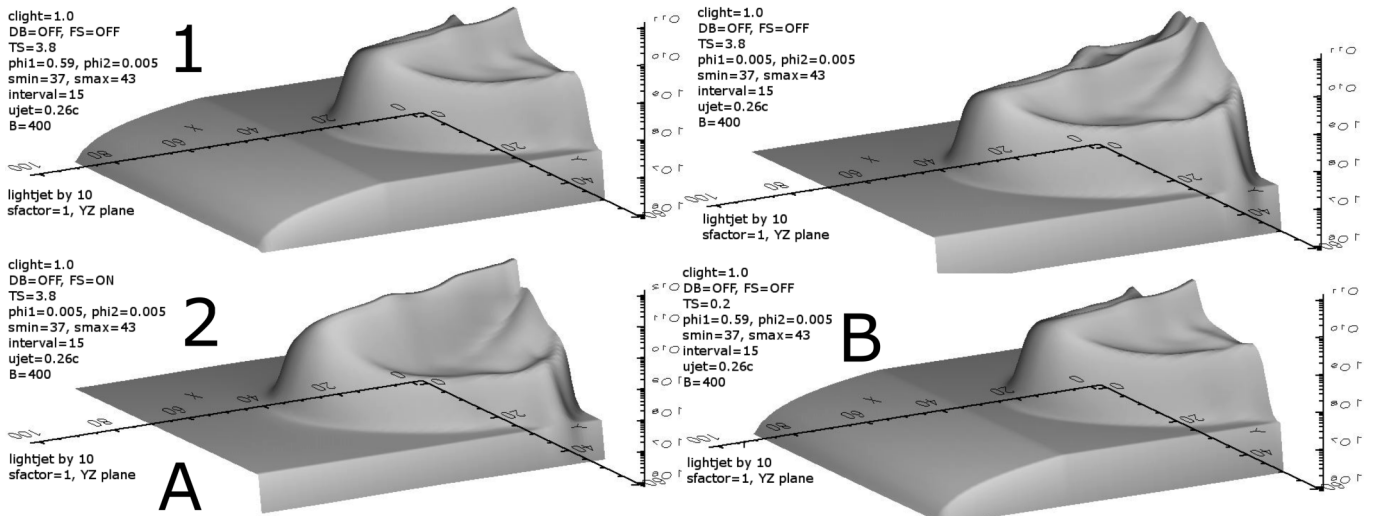


FIGURE 12. First part of the third batch of the results.

(process4,page1,2A,ts=1.0,clight=1,a1=0.45,a2=0.35,DB=on,FS=off,B=400,smin=18,smax=23, ujet=0.6c,YZ plane,shotmax=4,interval=15,sfactor=1,lightby10)

Comment: Angle 2 is varied here, at a large angle 1. Consequently, the view is rotated around a direction non-parallel to the jet, resulting to quite large differences between the two images (Section 2.2.3).

A pair. (process4,page1,1B,ts=1.0,clight=1,a1=0.005,a2=0.35,DB=on,FS=off,lightby10,smin=18, smax=23,ujet=0.6c,YZ plane,shotmax=4,sfactor=1,B=400,interval=15) vs (process4,page1,2B,ts=1.0,clight=1,a1=0.005,a2=0.005,DB=on,FS=off,lightby10,smin=18,smax=23, ujet=0.6c,YZ plane,shotmax=4,sfactor=1,B=400,interval=15)

TIME-RESOLVED JET IMAGING

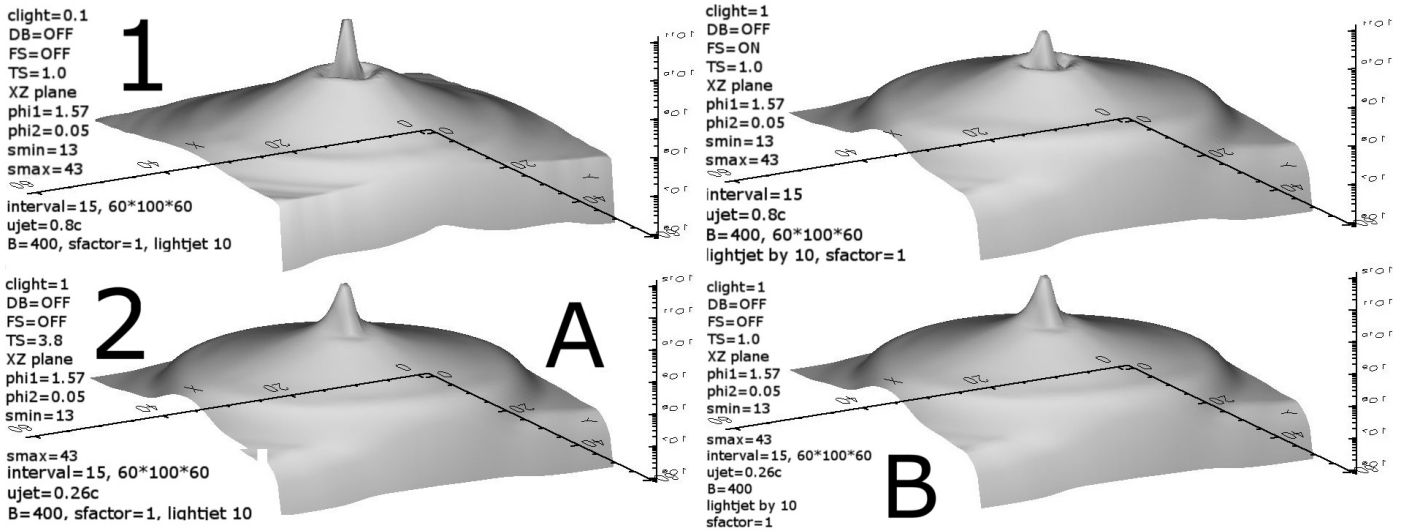


FIGURE 13. Second part of the third batch of the results.

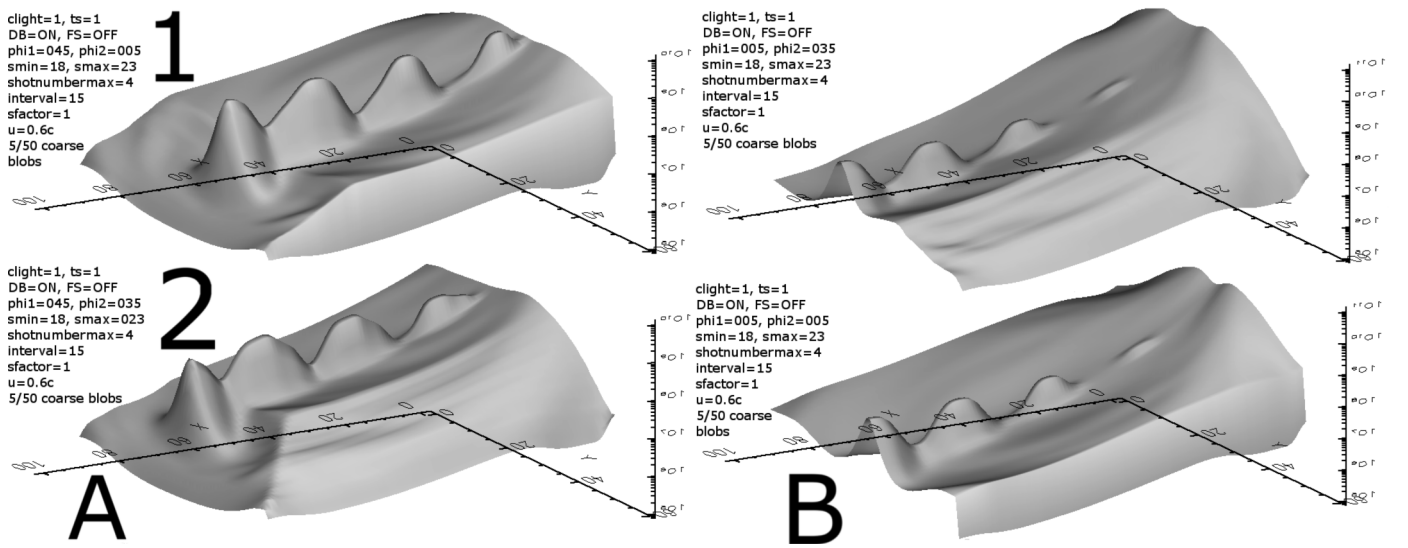


FIGURE 14. First part of the fourth batch of the results.

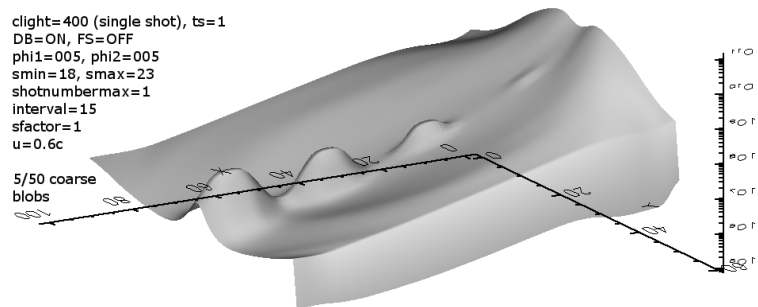


FIGURE 15. Second part of the fourth batch of the results.

Comment: Angle 2 is varied here, this time at a *small* angle 1. As a result, the view is rotated around a direction nearly parallel to the jet, resulting to much smaller differences between the two images, as compared to the previous pair.

4.3. Frequency shift

The FS facility is explored here.

A pair. (process2,page3,1A,clight=1,ts=1.0,a1=0.005,a2=0.005,DB=yes,FS=no,smin=37,smax=43,ujet=0.26c,YZ plane,interval=15,sfactor=1,lightby10,B=400) vs (process2,page3,2A,clight=1,ts=1.0,a1=0.005,a2=0.005,DB=yes,FS=yes,smin=37,smax=43,ujet=0.26c,YZ plane,interval=15,sfactor=1,lightby10,B=400)

Comment: Here the images look almost the same, any small differences that might occur being located mainly along the jet axis. At such a low jet speed and with the LOS nearly perpendicular to the jet, the $1/D^2$ effect of FS is limited, resulting to a couple of very similar images.

A pair. (process2,page3,1B,clight=1,ts=3.8,a1=0.005,a2=0.005,DB=yes,FS=no,smin=37,smax=43,ujet=0.26c,YZ plane,interval=15,sfactor=1,lightby10,B=400) vs (process2,page3,2B,clight=1,ts=3.8,a1=0.005,a2=0.005,DB=yes,FS=yes,smin=37,smax=43,ujet=0.26c,YZ plane,interval=15,sfactor=1,lightby10,B=400)

Comment: These two images look the same everywhere, except a slight difference along the jet axis. There, the intensity is slightly raised when FS is switched on. At such low angles, losu is almost $\pi/2$ and coslosu tends to zero, clearly outside the Doppler boost cone. Combined with such a high effective jet speed ($\text{ts}=3.8$), the resulting Doppler factor D is quite smaller than 1. Consequently, 'losing' two D factors when FS is turned *on* (Section 2.4.5, case 2 vs case 1) lead to a detectable increase in emission along the jet axis. Elsewhere, velocities are lower and the differentiating effect of FS is much weaker.

4.4. Doppler boosting

A pair. (process2,page2,2A,clight=1,ts=3.8,YZ plane,smin=37,smax=43,ujet=0.26c,B=400,a1=0.59,a2=0.005,DB=yes,FS=no,lightby10, interval=15,sfactor=1) vs (process3,page1,1A,clight=1,ts=3.8,YZ plane,smin=37,smax=43,ujet=0.26c,B=400,a1=0.59,a2=0.005,DB=no,FS=no,lightby10,interval=15,sfactor=1)

Comment: Despite a difference in their z axis maxima, the two images in this pair are quite similar, apart from the jet axis region. At such a high effective velocity ($\text{ts} \times c \simeq 0.988$), the boost cone is narrow, therefore the angle 1 value of 0.59 rad places the LOS outside the aforementioned cone, de-boosting the jet when DB is turned on. Consequently, intensity in this pair is actually higher without DB.

A pair. (process2,page2,2B,clight=1,ts=0.2,YZ plane,smin=37,smax=43,ujet=0.26c,B=400,a1=0.59,a2=0.005,DB=yes,FS=no,lightby10,interval=15,sfactor=1) vs (process3,page1,2B,clight=1,ts=0.2,YZ plane,smin=37,smax=43,ujet=0.26c,B=400,a1=0.59,a2=0.005,DB=no,FS=no,lightby10,interval=15,sfactor=1)

Comment: In this case, the two images look very similar, since at such a low ts factor, the effective maximum velocity is $0.26c \times 0.2 = 0.052c$, leading to very little relativistic boosting or de-boosting, despite the far from zero value of angle 1.

A pair. (process2,page3,1B,clight=1,ts=3.8,YZ plane,smin=37,smax=43,ujet=0.26c,B=400,a1=0.005,a2=0.005,DB=no,FS=no,lightby10,interval=15,sfactor=1) vs

TIME-RESOLVED JET IMAGING

(process3,page1,1B,clight=1,ts=3.8,YZ plane,smin=37,smax=43,
u_{jet}=0.26c,B=400,a1=005,a2=0.005,DB=no,FS=no,lightby10,interval=15,sfactor=1)

Comment: The Doppler-boosted image is much weaker (de-boosting) along the jet axis, at an effective jet speed of $ts \times 0.26c = 0.988c$. To the sides, intensities differ much less, even at this high artificial velocity. The above are attributed to the boost cone being narrow enough to exclude from itself this pair's LOS direction, where both angles have near zero values.

A pair. (process1,page1,1A,clight=0.1,ts=1.0,XZplane,smin=13,smax=43,u_{jet}=0.8c,B=400,
a1=1.57,a2=0.05,DB=yes,FS=no,lightby10,interval=15,sfactor=1) vs
(process3,page2,1A,clight=0.1,ts=1.0,XZ plane,smin=13,smax=43,u_{jet}=0.8c,B=400,
a1=1.57,a2=0.05,DB=no,FS=no,lightby10,interval=15,sfactor=1)

Comment: The boosting effect is quite large in (1,1,1A), of the order of a thousand, since angle 1 approaches $\pi/2$, lying inside the boost cone, at $u_{jet(injected)}=0.8c$. When DB is turned on (1,1,1A), the jet base footprint appears narrower, limiting the area of stronger emission to the close vicinity of the jet axis. The reason is that speed now makes a difference and only the jet axis possesses it. In contrast, deactivating DB largely cancels the above narrowing effect of stronger emission to the vicinity of the jet axis. Furthermore, the 'dark ring' of reduced emission, surrounding the jet axis (3,2,1A), represents an area vacated by the winds being pushed away to the sides and is present only in the fast jet model run.

The reader should also notice that these images are drawn at low clight (0.1), meaning the rays advance at 1/10 of their normal speed, thus drawing the image employs many snapshots, beginning early in the model run (smin=13). A narrower jet projection results, since the slower LOS reaches *later* snapshots, when the winds around the jet base have been pushed away and therefore diluted by the jet effects. In general, intensity contributions from the jet base, earlier on in the timeline, add more to the final result.

A pair. (process1,page1,2A,clight=1,ts=3.8,XZ plane,smin=13,smax=43,u_{jet}=0.26c,B=400,
a1=1.57,a2=0.05,DB=yes,FS=no,lightby10,interval=15,sfactor=1) vs
(process3,page2,2A,clight=1,ts=3.8,XZ plane,smin=13,smax=43,u_{jet}=0.26c,B=400,
a1=1.57,a2=0.05,DB=no,FS=no,lightby10,interval=15,sfactor=1)

Comment: A similar case appears here, where the boosted jet looks stronger but narrower, while the de-boosted one is wider than before. This time the effective jet speed is $0.988c$, the result of multiplying u_{jet} and ts .

A pair. (process1,page1,2B,clight=1,ts=1.0,XZ plane,smin=13,smax=43,u_{jet}=0.26c,B=400,
a1=1.57,a2=0.05,DB=yes,FS=no,lightby10,interval=15,sfactor=1) vs
(process3,page2,2B,clight=1,ts=1.0,XZ plane,smin=13,smax=43,u_{jet}=0.26c,B=400,
a1=1.57,a2=0.05,DB=no,FS=no,lightby10,interval=15,sfactor=1)

Comment: In (1,1,2B, DB=on) we obtain some boosting, by 1.3 times approximately, at an effective speed of $0.26c$. Nevertheless, the two images differ considerably from each other. Employing DB significantly narrows the visible part of the jet base, while making it emit somehow stronger as well. On the other hand, turning DB off (3,2,2B), leads to a wider emission base for the jet, since now only density matters to the result.

4.5. Tweak speed

In this subsection we explore the effects, on the synthetic image, of artificially altering, on a global scale, in post-processing, the matter speed.

A pair. (process1,page1,2A,clight=1,ts=3.8,XZ plane,smin=13,smax=43,ujet=0.26c,B=400, a1=1.57,a2=0.05,DB=yes,FS=no,lightby10,interval=15,sfactor=1) vs
(process1,page1,2B,clight=1,ts=1.0,XZ plane,smin=13,smax=43,ujet=0.26c,B=400, a1=1.57,a2=0.05,DB=yes,FS=no,lightby10,interval=15,sfactor=1)

Comment: Both images of this pair are Doppler boosted. At a higher effective speed, by 3.8 times, meaning 0.988c, we observe an emission increase by about one hundred times (1,1,2A), relative to the image drawn at the natural speed (1,1,2B). The intensity profile, moving from the jet periphery radially towards its axis, is steeper, spanning 7 orders of magnitude, for the artificially faster jet. On the other hand, for the slower jet, the corresponding radial intensity profile only spans 5 orders of magnitude.

A quartet. (process2,page2,1A,clight=1,ts=1.8,YZ plane,smin=37,smax=43,ujet=0.26c,B=400, a1=0.59,a2=0.005,DB=yes,FS=no,lightby10,interval=15,sfactor=1) vs
(process2,page2,1B,clight=1,ts=1.0,YZ plane,smin=37,smax=43,ujet=0.26c,B=400, a1=0.59,a2=0.005,DB=yes,FS=no,lightby10,interval=15,sfactor=1) vs
(process2,page2,2A,clight=1,ts=3.8,YZ plane,smin=37,smax=43,ujet=0.26c,B=400, a1=0.59,a2=0.005,DB=yes,FS=no,lightby10,interval=15,sfactor=1) vs
(process2,page2,2B,clight=1,ts=0.2,YZ plane,smin=37,smax=43,ujet=0.26c,B=400, a1=0.59,a2=0.005,DB=yes,FS=no,lightby10,interval=15,sfactor=1)

Comment: At an angle θ of 0.59 rad, some Doppler boosting ($1 \leq D \leq 2$, see also Section 4.6) is present along the jet axis at $ts = 0.2, 1.0$ and 1.8 (effective maximum jet speed of $0.052c, 0.26c$ and $0.468c$ respectively). At $ts=3.8$ though ($0.988c$), no boosting occurs along the jet. This means that the higher the effective jet speed, the narrower the boost cone, eventually leaving out of it the losu angle corresponding to angle θ of .59 rad.

A pair. (process2,page3,1A,clight=1,ts=1.0,YZ plane,smin=37,smax=43,ujet=0.26c,B=400, a1=0.005,a2=0.005,DB=yes,FS=no,lightby10,interval=15,sfactor=1) vs
(process2,page3,1B,clight=1,ts=3.8,YZ plane,smin=37,smax=43,ujet=0.26c,B=400, a1=0.005,a2=0.005,DB=yes,FS=no,lightby10,interval=15,sfactor=1)

Comment: At an effective speed of $0.988c$ (2,3,1B), the boost cone is pretty narrow, therefore at such small angles θ 1 and 2 (meaning losu approaches $\pi/2$ and $\cos\theta$ nears zero), the jet appears de-boosted, along its axis. On the other hand, at an effective speed of $0.26c$ (2,3,1A) the jet axis still emits significantly, at an approximate value of $D(u=0.26c, \cos\theta=0) \simeq 0.8$.

A pair. (process2,page3,2A,clight=1,ts=1.0,YZ plane,smin=37,smax=43,ujet=0.26c,B=400, a1=0.005,a2=0.005,DB=yes,FS=yes,lightby10,interval=15,sfactor=1) vs
(process2,page3,2B,clight=1,ts=3.8,YZ plane,smin=37,smax=43,ujet=0.26c,B=400, a1=0.005,a2=0.005,DB=yes,FS=yes,lightby10,interval=15,sfactor=1)

Comment: A situation similar to the previous pair, only this time FS is turned on. At high effective velocities, de-boosting occurs, essentially along the jet axis. Compared to the previous pair, Doppler effects are less intense in both images here, now being proportional to $D^{1+\alpha}$, as opposed to $D^{3+\alpha}$ in the previous group of two. Consequently, this pair's 'fast' jet, (2,3,2B), now has more intensity than the corresponding one of the previous pair (2,3,1B), since now De-boosting is smaller.

A pair. (process3,page1,1A,clight=1,ts=3.8,YZ plane,smin=37,smax=43,ujet=0.26c,B=400, a1=0.59,a2=0.005,DB=no,FS=no,lightby10,interval=15,sfactor=1) vs
(process3,page1,2B,clight=1,ts=0.2,YZ plane,smin=37,smax=43,ujet=0.26c,B=400, a1=0.59,a2=0.005,DB=no,FS=no,lightby10,interval=15,sfactor=1)

TIME-RESOLVED JET IMAGING

Comment: Despite a huge difference in effective speeds, still no apparent difference, since both DB and FS are turned off. The only factor left affecting intensity is matter density, which is identical for both images.

A pair. (process3,page2,2A,clight=1,ts=3.8,XZ plane,smin=13,smax=43,ujet=0.26c,B=400, a1=1.57,a2=0.05,DB=no,FS=no,lightby10,interval=15,sfactor=1) vs
(process3,page2,2B,clight=1,ts=1.0,XZ plane,smin=13,smax=43,ujet=0.26c,B=400, a1=1.57,a2=0.05,DB=no,FS=no,lightby10,interval=15,sfactor=1)

Comment: A higher speed tweak (3,2,2A) normally leads to enhanced effects of DB and FS, especially when the LOS is almost parallel to the jet, as is the case with this pair. But here, both DB and FS are turned *off*. Consequently, no apparent difference occurs between the two images.

4.6. Clight

Varying the clight parameter directly affects the temporal rate of advance of the LOS through the 4D data arrays. Relativistic calculations of the Lorentz and Doppler factors remain unaffected though.

A pair. A pair where time-resolved imaging is explored, as caused by including many temporal shots (1,1,1A, clight=0.1) vs using just a few (1,1,1B, clight=1.0).

(process1,page1,1A,clight=0.1,ts=1.0,XZ plane,smin=13,smax=43,ujet=0.8c,B=400, a1=1.57,a2=0.05,DB=yes,FS=no,lightby10,interval=15,sfactor=1) vs
(process1,page1,1B,clight=1.0,ts=1.0,XZ plane,smin=13,smax=43,ujet=0.8c,B=400, a1=1.57,a2=0.05,DB=yes,FS=no,lightby10,interval=15,sfactor=1)

Comment: We can see here the difference slow-light relativistic imaging (1,1,1A) makes, pertaining to the final result, compared to simply imaging at normal light speed (1,1,1B). The 'slow' image, formed as a combination of a longer series of snapshots, still appears quite natural to the eye, perhaps resembling an intermediate time instant in the jet evolution. The slower the imposed speed of light, the less laterally developed the jet emission appears (1,1,1A), as later snapshots have less to contribute to the final result (later on, surrounding winds' density, as projected on XZ, around the jet base, tends to fade).

A quartet. (process2,page1,2A,clight=400,ts=1.0,YZ plane,smin=13,smax=43,ujet=0.26c,B=400, a1=0.005,a2=0.005,DB=yes,FS=no,lightby10,interval=15,sfactor=1) vs
(process2,page1,2B,clight=0.1,ts=1.0,YZ plane,smin=13,smax=43,ujet=0.26c,B=400, a1=0.005,a2=0.005,DB=yes,FS=no,lightby10,interval=15,sfactor=1) vs
(process2,page1,1A,clight=400,ts=1.0,YZ plane,smin=31,smax=43,ujet=0.26c,B=400, a1=0.005,a2=0.005,DB=yes,FS=no,lightby10,interval=15,sfactor=1) vs
(process2,page1,1B,clight=400,ts=1.0,YZ plane,smin=42,smax=43,ujet=0.26c,B=400, a1=0.005,a2=0.005,DB=yes,FS=no,lightby10,interval=15,sfactor=1)

Comment: The effect of slowing down light, by a factor of 10 times (2,1,2B), is compared to three effectively single shot images (clight = 400), taken at different time instants (smin \times interval). The jet traverses a substantial portion of the computational grid during the formation of the 'slow light' synthetic image, as compared to the earliest snapshot of this group (2,1,2A). Still, the final result appears quite natural to the eye, resembling an intermediate snapshot, between (2,1,1A) and (2,1,1B).

A pair. A similar test.

(process4,page1,2B,clight=1,ts=1.0,YZ plane,smin=13,smax=43,ujet=0.6c,B=400, a1=0.005,a2=0.005,DB=yes,FS=no,lightby10,interval=15,sfactor=1) vs

(process4,page2,clight=400,ts=1.0,YZ plane,smin=18,smax=23,ujet=0.6c,B=400,
a1=0.005,a2=0.005,DB=yes,FS=no,lightby10,interval=15,sfactor=1)

Comment: In the time-resolved image (4,1,2B), the 4th blob has exited the grid by about half its length. On the other hand, in the single shot image (4,2), most of the 4th blob is still within the grid.

4.7. Time instant

A series of snapshots are compared here.

(process2,page1,1A,clight=400,ts=1.0,YZ plane,smin=31,smax=43,ujet=0.26c,B=400,
a1=0.005,a2=0.005,DB=yes,FS=no,lightby10,interval=15,sfactor=1) vs

(process2,page1,2A,clight=400,ts=1.0,YZ plane,smin=42,smax=43,ujet=0.26c,B=400,
a1=0.005,a2=0.005,DB=yes,FS=no,lightby10,interval=15,sfactor=1) vs

(process2,page1,1B,clight=400,ts=1.0,YZ plane,smin=42,smax=43,ujet=0.26c,B=400,
a1=0.005,a2=0.005,DB=yes,FS=no,lightby10,interval=15,sfactor=1)

Comment: This is merely a comparison between three single-shot images, taken at different time instants, all other parameters being the same. The jet has advanced considerably among the three snapshots.

4.8. Mixed parameters

In this subsection we simultaneously alter more than one imaging parameters, in order to study their combined effects on the output.

ts and jet injection speed (I). ts and jet injection speed both change here:

(process1,page1,2A,clight=1.0,ts=3.8,XZ plane,smin=13,smax=43,ujet=0.8c,B=400,
a1=1.57,a2=0.05,DB=yes,FS=no,lightby10,interval=15,sfactor=1) vs

(process1,page1,1B,clight=1.0,ts=1.0,XZ plane,smin=13,smax=43,ujet=0.8c,B=400,
a1=1.57,a2=0.05,DB=yes,FS=no,lightby10,interval=15,sfactor=1)

Comment: In this pair, a jet injection speed of 0.8c is compared to a jet injection speed of 0.26c raised artificially, for Doppler boosting calculation purposes, to 0.988c. The 0.8c jet (1,1,1B) is therefore dynamically more developed, but it is less boosted radiatively, since the slower jet (1,1,2A) is artificially assigned a higher velocity.

ts and jet injection speed (II). (process3,page2,1B,clight=1.0,ts=1.0,XZ plane,smin=13,
smax=43,ujet=0.8c,B=400,a1=1.57,a2=0.05,DB=no,FS=yes,lightby10,interval=15,sfactor=1) vs
(process3,page2,2A,clight=1.0,ts=3.8,XZ plane,smin=13,smax=43,ujet=0.26c,B=400,
a1=1.57,a2=0.05,DB=no,FS=no,lightby10,interval=15,sfactor=1)

In the vicinity of the jet base, for the dynamically faster jet (3,2,1B), a drop in intensity occurs, the surrounding winds being pushed aside more. On the other hand, (3,2,2A) features a slightly higher maximum intensity, thanks to its effective speed being higher (0.988c vs 0.8c), even though its actual speed is much lower (0.26c).

clight and FS. clight and FS both change here:

(process3,page2,1A,clight=0.1,ts=1.0,XZ plane,smin=13,smax=43,ujet=0.8c,B=400,
a1=1.57,a2=0.05,DB=no,FS=no,lightby10,interval=15,sfactor=1) vs

(process3,page2,1B,clight=1.0,ts=1.0,XZ plane,smin=13,smax=43,ujet=0.8c,B=400,
a1=1.57,a2=0.05,DB=no,FS=yes,lightby10,interval=15,sfactor=1)

Comment: At such a high value of angle 1, the angle losu is near zero, and Doppler factor D takes substantial values. Furthermore, DB is turned off in this pair. Thereupon, the FS switch, reducing

TIME-RESOLVED JET IMAGING

intensity by D^2 , leads to less overall intensity in (3,2,1B), compared to (3,2,1A). On the other hand, emission from the region surrounding the jet base in (3,2,1A) appears weaker, since a slower effective speed of light allows later snapshots (jet base rarefied, pushed away by jet) to also contribute to the image. In the absence of DB, both images feature a 'ring' of reduced emission around the jet base, attributed to a jet 'cocoon' rarefied by the 0.8c jet.

5. Conclusions

RLOS has been evolved from its classical ancestor LOS code, in order to formulate an approximate solution to the problem of imaging model relativistic astrophysical jets. Despite its theoretical simplifications, the program succeeds in providing a time-delayed synthetic image of a hydrodynamical model jet, while avoiding the complexity of a more complete approach. Applications may include a variety of dynamical astrophysical phenomena, where synthetic observations are compared to actual ones, an achieved match largely validating the initial conditions of the numerical models.

RLOS tests verify the integrity of the program and demonstrate its versatility, when imaging a model astrophysical system. We also note its ability to incorporate various emission and absorption coefficients, either directly, by hardwiring the relevant formulae, or indirectly, for example by first exporting hydrocode data to other suitable mathematical programs, calculating there the coefficients globally, and then importing those back to RLOS. It is therefore possible to model emissions in many different wavebands, from radio to γ -rays. As an example, an X-ray synchrotron emission and self-absorption model may include a direct dependence of emission on the frequency shift effect. What's more, the use of a hydrocode allows modelling complex dynamical systems, facilitating the study of a wide range of situations.

Furthermore, apart from the currently employed emission dependence on density, emission may also be a function of the magnetic field, local velocity, and others. Certain particle emissions may even be included, if suitable directional relativistic expressions are employed, transforming emission from the jet to the stationary frames of reference. The inclusion of aberration is a potential next step in the program development, along with certain gravitational corrections to the ray path.

Bibliography

- [1] T. V. Cawthorne. In Hughes, editor, *Beams and Jets in Astrophysics*. Cambridge University Press, 1991.
- [2] R. J. Deissler. *Am. J. Phys.*, 73:663, 2005.
- [3] F. R. Hickey. *Am. J. Phys.*, 47:711, 1979.
- [4] R. M. Hjellming and K. J. Johnston. *ApJ*, 328:600, 1988.
- [5] P.K. Hsiung and R.H.P. Dunn. *Proceedings of Supercomputing 1989 Conference*, 1:597, 1989.
- [6] P.K. Hsiung, R.H. Thibadeau, and M. Wu. *Computer Graphics 24(2)*, 24:83, 1990.
- [7] P. A. Hughes. In Hughes, editor, *Beams and Jets in Astrophysics*. Cambridge University Press, 1991.
- [8] A. Jarabo, B. Masia, A. Velten, C. Barsi, R. Raskar, and D. Gutierrez. *Computer Graphics Forum*, 34 (8), 34:1, 2015.
- [9] R. D. Klauber. Is detection of fitzgerald-lorentz contraction possible? arXiv:0808.1117v1, 2008.

- [10] Gerd Kortemeyer, Philip Tan, and Steven Schirra. A slower speed of light: Developing intuition about special relativity with games fdg 2013. *FDG 13 Proceedings of the International Conference on the Foundations of Digital Games. ACM New York, NY, USA*, 1:400, 2013.
- [11] O. Kosmas and T. Smponias. AHEP accepted, 2018.
- [12] U. Kraus. *American Journal of Physics*, 68:56, 2000.
- [13] R. Laing and A. H. Bridle. Relativistic models and the jet velocity field in the radio galaxy 3c 31. *Monthly Notices of the Royal Astronomical Society*, 336:328, 2002.
- [14] A. Lampa. *Zeitschrift fur Physik*, 27:138, 1924.
- [15] A. Mignone, G. Bodo, S. Massaglia, T. Matsakos, O. Tesileanu, C. Zanni, and A. Ferrari. *Ap. J. Supp.*, 170:228, 2007.
- [16] I. F. Mirabel and L. F. Rodríguez. *Ann. Rev. Astron. Astrophys*, 37:409, 1999.
- [17] T. Muller. *Comput. Phys. Commun.*, 185:2301, 2014.
- [18] T. Muller and S. Boblest. *Eur. J. Phys.*, 35:06502, 2014.
- [19] R. Penrose. *Proc. Cambridge Phil. Soc.*, 55:137, 1959.
- [20] G. B. Rybicki and A. P. Lightman. *Radiative Processes in Astrophysics*. Wiley-Interscience, New York, 1979.
- [21] G. D. Scott and M. R. Viner. *American Journal of Physics*, 33:534, 1965.
- [22] Z. W. Sherin, R. Cheu, P. Tan, and G. Kortemeyer. Visualizing relativity: the openrelativity project. *American Journal of Physics*, 84:369, 2016.
- [23] T. Smponias and O. Kosmas. *Advances in High Energy Physics*, 921757, 2015.
- [24] T. Smponias and O. Kosmas. *Advances in High Energy Physics*, 4962741, 2017.
- [25] T. Smponias and T. S. Kosmas. *MNRAS*, 412:1320, 2011.
- [26] T. Smponias and T. S. Kosmas. *MNRAS*, 438:1014, 2014.
- [27] W. B. Sparks, D. Fraix-Burnet, F. Macchetto, and F. N. Owen. A counterjet in the elliptical galaxy m87. *Nature*, 355:804, 1992.
- [28] J. Terrell. *Phys. Rev.*, 116:1041, 1959.
- [29] A. Velten, D. Wu, A. Jarabo, B. Masia, C. Barsi, C. Joshi, E. Lawson, M. Bawendi, D. Gutierrez, and R. Raskar. *ACM Trans. Graph.*, 32:4, 2013.
- [30] D. Weiskopf. *Dissertation*. PhD thesis, Dissertation, der Eberhard-Karls-Universität zu Tübingen, der Fakultät für Physik, 2001.
- [31] D. Weiskopf. In Hans Hagen, editor, *Scientific Visualization: Advanced Concepts*, page 289302. Dagstuhl Publishing, Leibniz Center for Informatics, Germany, 2010.
- [32] D. Weiskopf, U. Kraus, and H. Ruder. *ACM Trans. Graph.*, 18:3, 1999.
- [33] V. F. Weisskopf. *Phys. Today*, 13:24, 1960.

TIME-RESOLVED JET IMAGING

Appendix A. Synthetic images enlarged

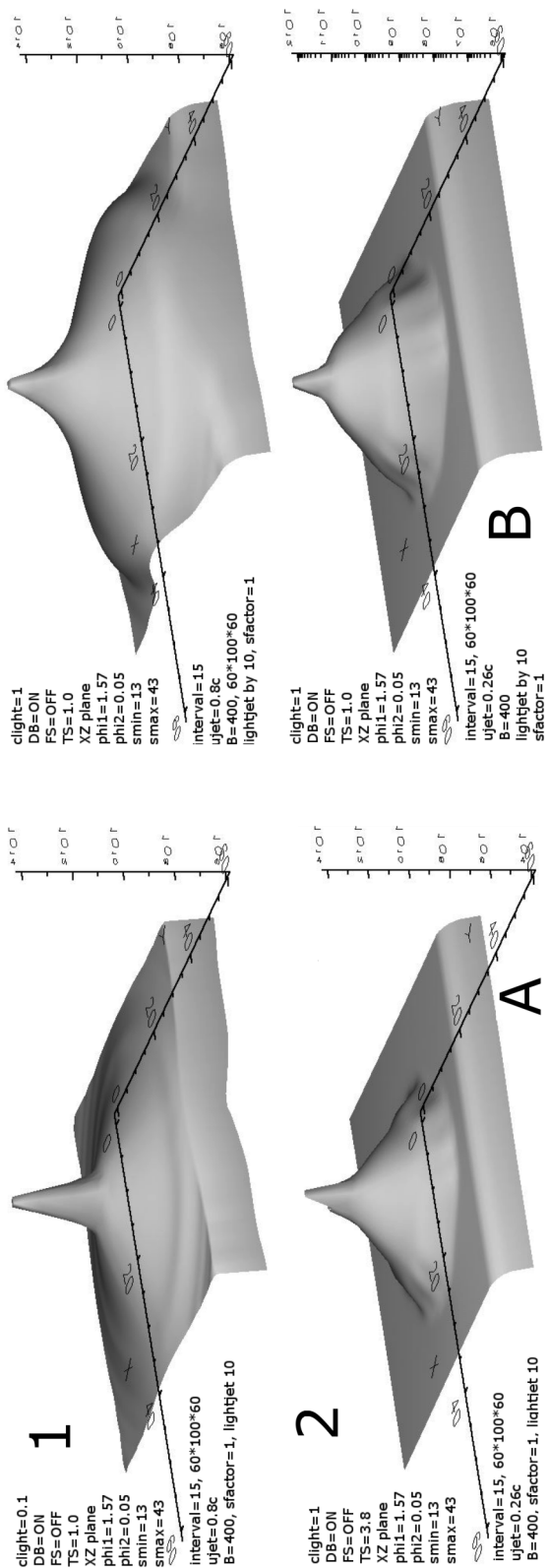


FIGURE 16. First and only part of the first batch of the results.

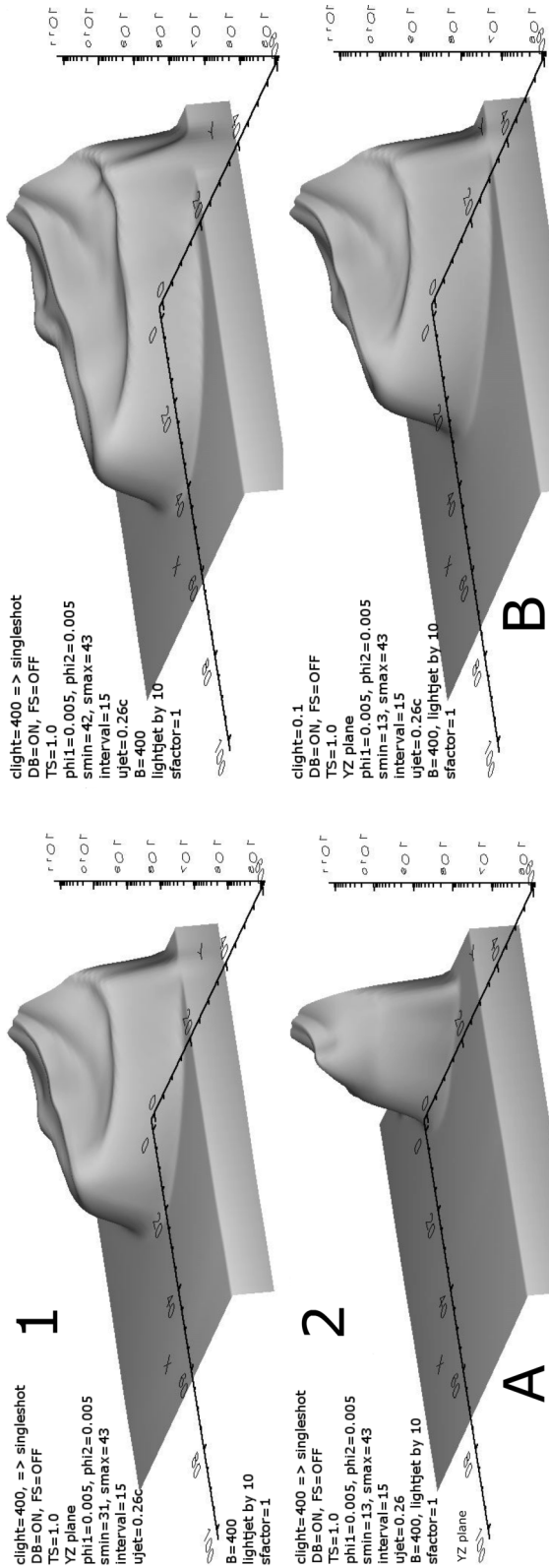


FIGURE 17. First part of the second batch of the results.

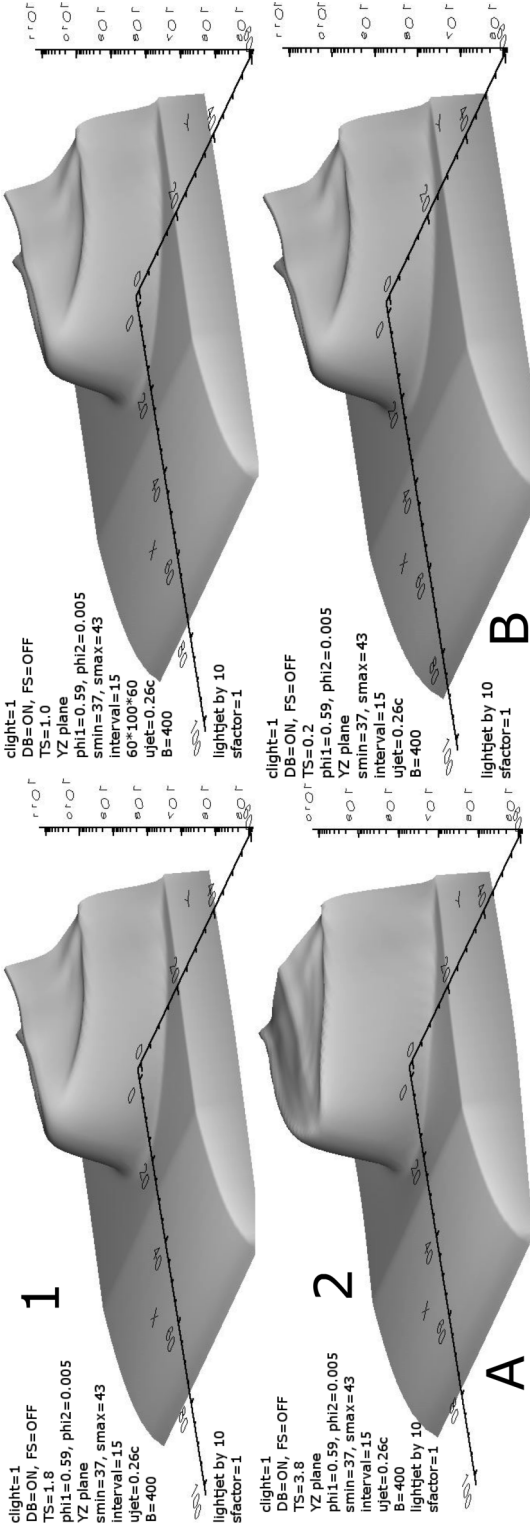


FIGURE 18. Second part of the second batch of the results.

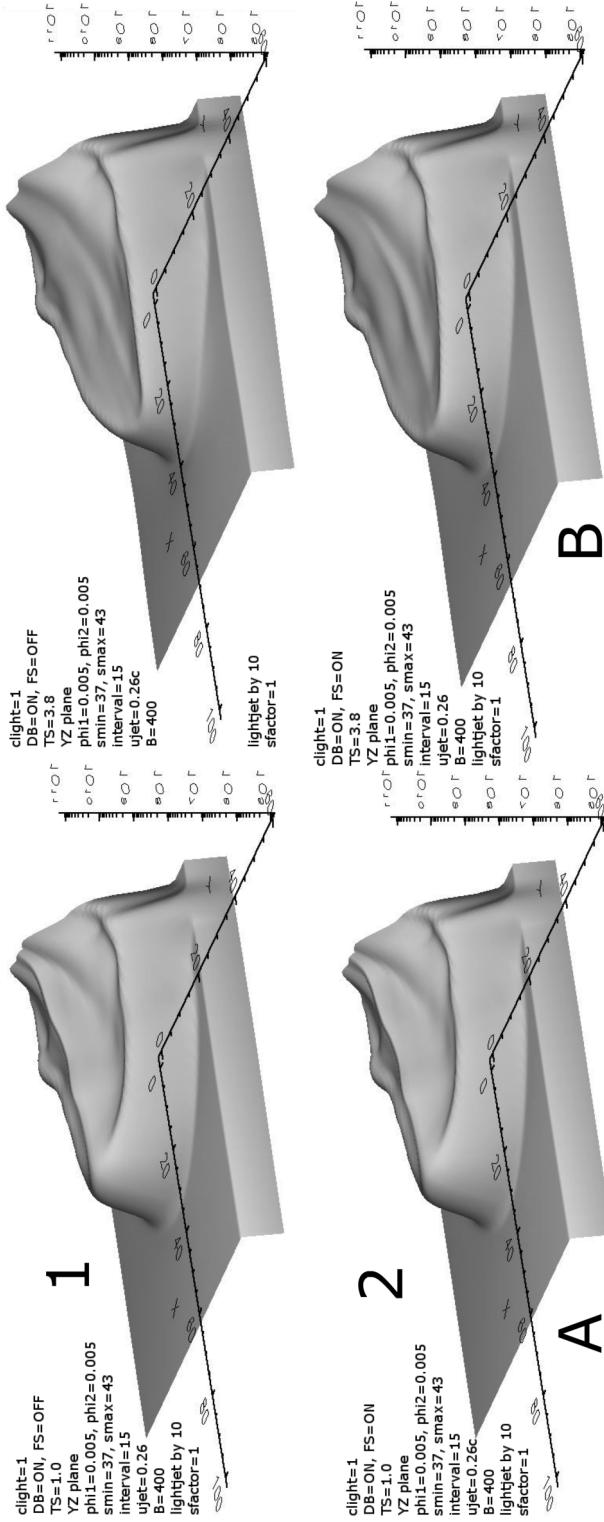


FIGURE 19. Third part of the second batch of the results.

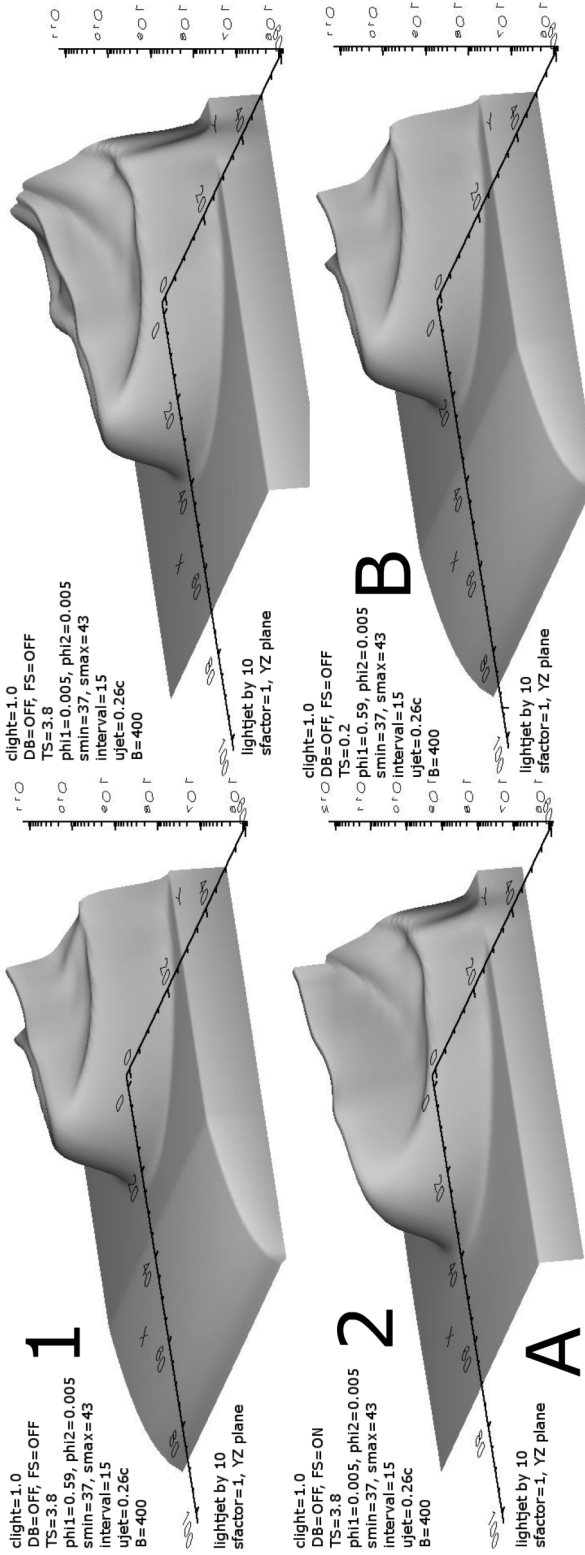


FIGURE 20. First part of the third batch of the results.

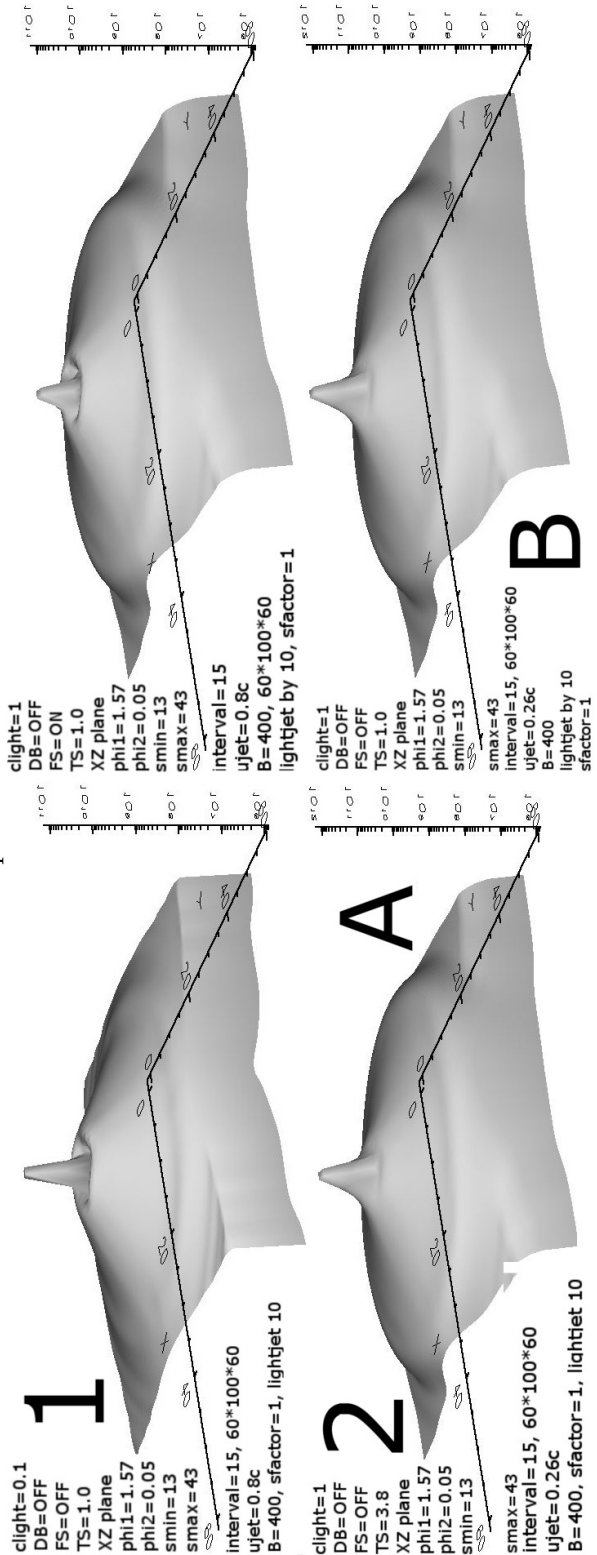


FIGURE 21. Second part of the third batch of the results.

TIME-RESOLVED JET IMAGING

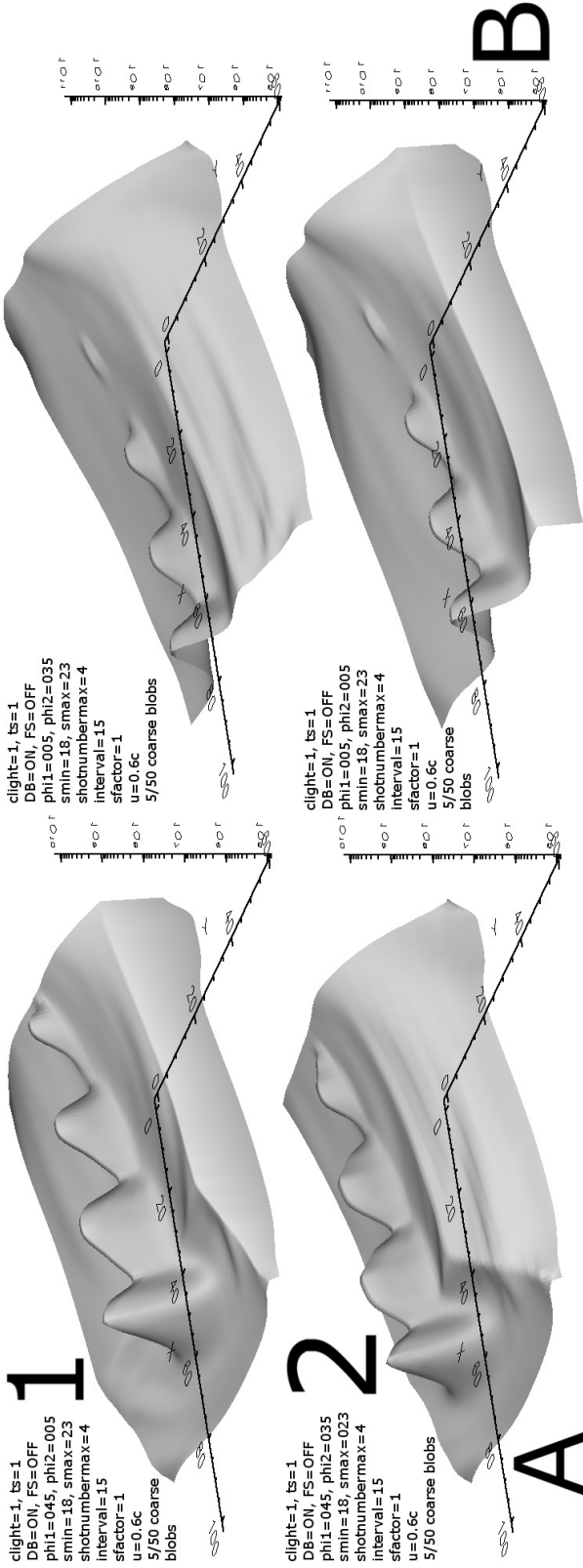


FIGURE 22. First part of the fourth batch of the results.

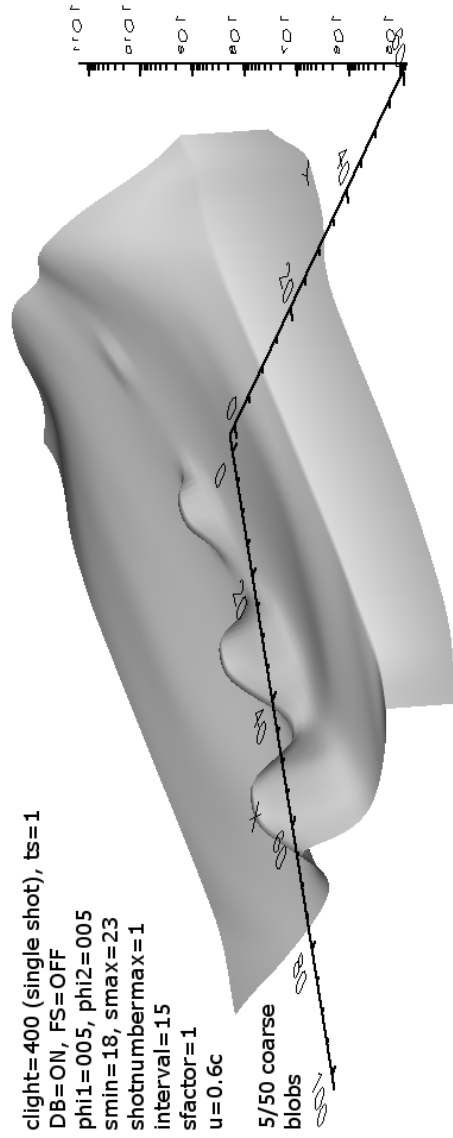


FIGURE 23. Second part of the fourth batch of the results.